SPATIOTEMPORAL PATTERNS IN A REACTION-DIFFUSION SYSTEM AND IN A VIBRATED GRANULAR BED

Harry L. Swinney, K. J. Lee, W. D. McCormick, F. Melo, and P. Umbanhowar

Center for Nonlinear Dynamics and Department of Physics
The University of Texas at Austin
Austin, Texas 78712

ABSTRACT

Experiments on a quasi-two-dimensional reaction-diffusion system reveal transitions from a uniform state to stationary hexagonal, striped, and rhombic spatial patterns. For other reactor conditions lamellae and self-replicating spot patterns are observed. These patterns form in continuously fed thin gel reactors that can be maintained indefinitely in well-defined nonequilibrium states. Reaction-diffusion models with two chemical species yield patterns similar to those observed in the experiments. Pattern formation is also being examined in vertically oscillated thin granular layers (typically 3-30 particle diameters deep). For small acceleration amplitudes, a granular layer is flat, but above a well-defined critical acceleration amplitude, spatial patterns spontaneously form. Disordered time-dependent granular patterns are observed as well as regular patterns of squares, stripes, and hexagons. A one-dimensional model consisting of a completely inelastic ball colliding with a sinusoidally oscillating platform provides a semi-quantitative description of most of the observed bifurcations between the different spatiotemporal regimes.

INTRODUCTION

We are examining the formation of spatiotemporal patterns in two types of far-from-equilibrium systems that have been chosen in part because of their potential applications: (1) reaction-diffusion systems maintained by a continuous feed of chemicals, and (2) vertically oscillated thin layers of granular materials. Our earlier work on spatially extended chemical reactors demonstrated that in some cases a pattern forming chemical system can be used to achieve higher yield of certain species than can be achieved in the standard well-stirred batch or continuous flow (CSTR) reactors [1-2].

Shallow layers of granular materials ("vibrated beds") are used in industry because of their good heat and mass transfer properties [3-4]. A previous study observed square patterns in a vibrated bed [3], but the present work is the first to investigate systematically pattern formation in these systems.

Our goal is to understand the fundamental mechanisms leading to pattern formation and to determine the properties and parameter ranges of the different patterned regimes. Precision computer-controlled reactors and vibrated beds have been developed for these studies, and a high degree of reproducibility, unprecedented for these systems, is being achieved. The experiments are complemented by studies of models that provide insight into the spatiotemporal dynamics.

REACTION-DIFFUSION PATTERNS

Turing patterns

In a classic 1952 paper, Turing predicted that patterns could spontaneously form in reaction-diffusion systems. Turing considered systems with diffusion and chemical kinetic processes but no convection. We have developed reactors in which patterns form in a thin gel layer — the (essentially inert) gel prevents convection [5-11]. The gel layer is in contact on one or both sides with continuously refreshed reservoirs of the reagents of the reaction; thus the system can be maintained indefinitely in a well-defined nonequilibrium state.

In a study of a chlorite-iodide-malonic acid reaction, we found that patterns emerge spontaneously from an initially uniform background when critical values of the control parameters (chemical concentrations, temperature, gel thickness) are exceeded: the primary bifurcation leads to hexagonal patterns, as shown in Fig. 1(a) [5,7]. The wavelength λ of Turing patterns is predicted to depend not on the geometry (as in, e.g., fluid dynamic patterns), but only on the properties of the system: $\lambda = (2\pi\tau D)^{1/2}$, where D and τ are, respectively, a characteristic molecular diffusion coefficient of the reacting species and a characteristic time determined by the chemical kinetics. We have recently made direct measurements of D and τ and have confirmed the predicted dependence of λ on D and τ [6].

Fig. 1. Stationary chemical patterns formed in continuously fed gel reactors: (a) hexagons [5-8], (b) stripes [5-8], and (c) lamellae [9-10]. The gels are thin compared to the wavelength of the patterns so the patterns are approximately two-dimensional. Patterns (a) and (b), each 1 mm x 1 mm, were observed in a chlorite-iodide-malonic acid reaction [7]; variations in darkness correspond to variations in concentration of triiodide. Pattern (c), 13 mm x 10 mm, was observed in a ferrocyanide-iodate-sulfite reaction [9].

At the onset of instability the patterns consist of regular hexagons with 60° angles between all dots neighboring another dot [see, e.g., Fig. 1(a)], but beyond the onset of instability the hexagons can be slightly squashed — e.g., the angles between neighboring dots can be 57°, 66°, 57°, 57°, 66°, 57°; such rhombic structures have been found to be a consequence of the translational, rotational, and reflection symmetry of continuous planar continua [8].

With further increase in control parameter, we observe a bifurcation from hexagonal to striped patterns (cf. Fig. 1(b)) [5,7], and with yet further increase in control parameter the patterns can become disordered in both space and time [12].

Lamellae

Experiments on a bistable ferrocyanide-iodate-sulfite reaction have revealed a new type of spatial pattern, one in which fronts propagate at a constant speed until they reach a critical separation (typically 0.4 mm in the experiments) and stop [9-10]. This behavior contrasts with the behavior of waves in excitable media, where colliding fronts annihilate one another. The front patterns develop locally and spread to fill space, resulting in a stationary asymptotic pattern that is highly irregular, as Fig. 1(c) illustrates. The pattern forming process also contrasts with that leading to the regular hexagonal and striped patterns (Fig. 1(a)-(b)), which emerge spontaneously everywhere in the medium when a critical control parameter value is exceeded: the lamellae must be initiated by a finite amplitude perturbation.

Self-replicating spots

For conditions close to those yielding lamellae, patterns of spots are observed and are found to undergo a continuous process of birth through replication and death through overcrowding, as Fig. 2 illustrates. The spots do not form spontaneously, but once initiated by a perturbation (UV light or a boundary perturbation), the spot patterns are self-sustaining. These patterns are observed for a wide parameter range in the ferrocyanide-iodate-sulfite reaction.

Models

Simulations of several different reaction-diffusion models with two chemical species have been found to yield lamellae and self-replicating spots similar to those observed in the experiments (see refs. in [10]). (Replicating spots were actually first found in a model [13]). Even abstract models that could describe convection and other pattern forming systems as well as chemical systems have been found to form lamellae like those in Fig. 2(c). Thus, while lamellae and replicating spots have not been observed in other laboratory systems maintained far from equilibrium, the occurrence of these patterns in several models suggests that there is nothing remarkable about our ferrocyanide-iodate-sulfite system — lamellar and spot patterns can be expected to form in other chemical systems and perhaps in non-chemical systems as well.

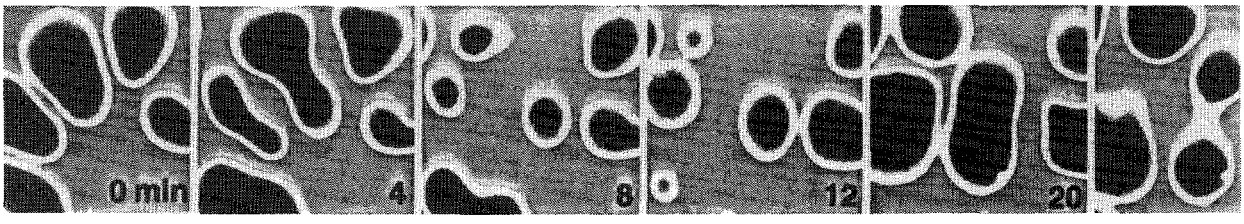

Fig. 2. Self-replicating spots evolving in time for 24 min. The behavior continues to evolve indefinitely as long as the reactor conditions are maintained [10-11]. Black represents the low pH state (pH ≅ 3); grey represents the high pH state (pH ≅ 7). The region shown is 7 mm x 7 mm.

PATTERNS IN VIBRATED GRANULAR BEDS

Granular materials are large assemblies of solid particles that interact mainly through nearest neighbor contacts; this is often a good approximation for granular systems in nature and industry, e.g., mined coal, concrete, cracking catalysts, rice, and pills. Granular materials comprise a unique state of matter with properties common to both fluids and solids. These shared properties make the application of statistical methods to the definition of mean quantities difficult, and cause phenomenological coefficients, such as viscosity or elasticity, to be strongly singular. Despite formidable challenges, the significant role of granular dynamics in industry and geology makes the understanding of these materials an important subject for science and engineering. Most research on granular materials has concerned static rather than dynamic properties, but in recent years some studies have begun to examine the time-dependent properties, and vibrating systems in particular have been found to exhibit some remarkable behavior [4, 14, 15].

The subject of our study, pattern formation in vibrated beds (shallow vertically oscillated layers), has not been previously examined in any detail [3-4]. We have found a variety of spatiotemporal patterns, some of which are illustrated in Fig. 3. We consider beds of particles that are sinusoidally oscillated with dimensionless acceleration amplitudes Γ in the range 0-9 (maximum acceleration relative to the gravitational acceleration) [16-17]. The particles (usually glass or bronze spheres in our experiments) have diameters in the range 0.1-1.0 mm. The layers are typically 3-30 particle diameters deep. The driving frequency ranges from 10 to 120 Hz. The container is 127 mm in diameter and 90 mm high. The container is evacuated to 0.1 torr, which is a pressure low enough so that volumetric effects of the remaining gas are negligible.

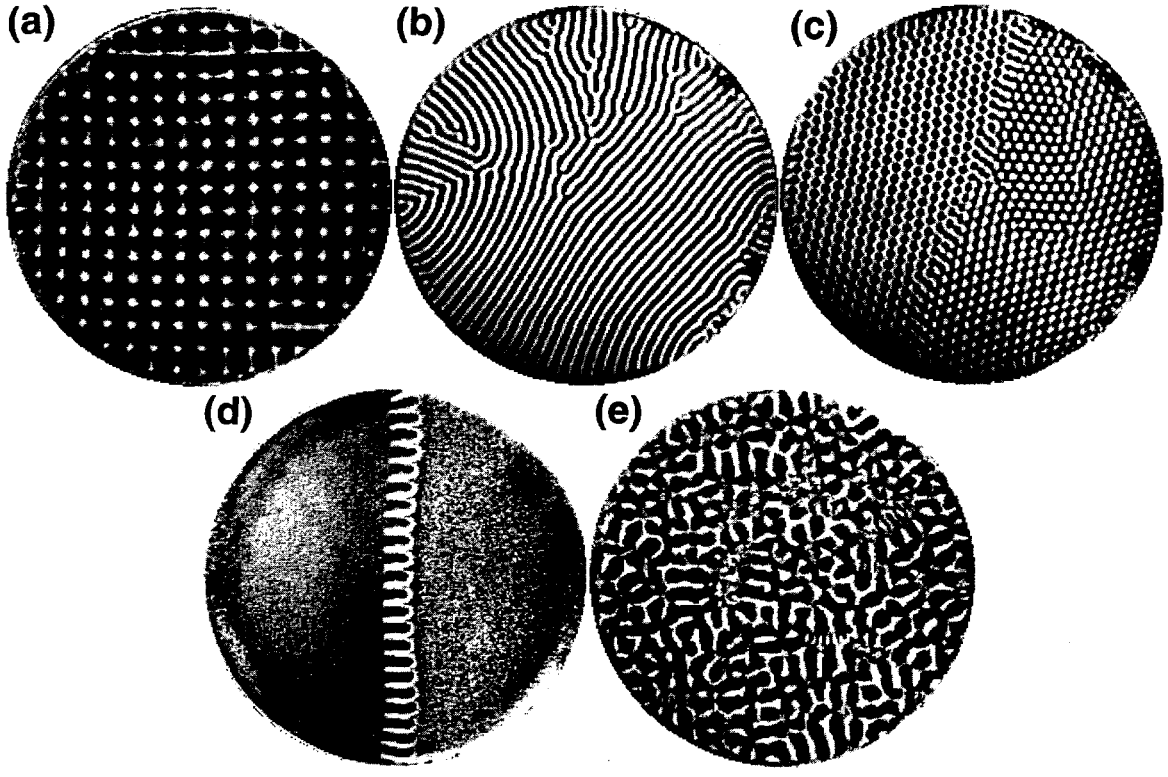

Fig. 3. Patterns observed for different dimensionless acceleration amplitudes Γ in a 1.2 mm thick layer of 0.15-0.18 mm diameter bronze spheres [16-17]: (a) squares (Γ = 2.7, f = 19 Hz), (b) stripes (Γ = 3.3, f = 67 Hz), (c) hexagons (Γ = 3.9, f = 67 Hz), (d) flat domains separated by kinks (Γ = 4.5, f = 37 Hz), and (e) disordered pattern (Γ = 8.5, f = 67 Hz).

We now describe some of the patterns.

Primary instability: squares and stripes

For small drive frequency f and increasing Γ, the flat surface bifurcates to a square standing wave pattern oscillating at f/2; see Fig. 3(a) [16-17]. For a drive frequency greater than a critical value (42 Hz for a 1.2 mm deep layer of 0.17 mm bronze spheres), the pattern is in the form of a stripes rather than squares, as Fig. 3(b) illustrates. The transition from a flat surface to squares is definitely hysteretic, while the hysteresis is small (perhaps absent) for the transition from a flat surface to a striped pattern.

Higher instabilities: hexagons, kinks, and disorder

As the acceleration is increased with the drive frequency fixed, we observe five successive regimes beyond the squares or stripes oscillating at f/2 (cf. Figs. 3 and 4) [17]: (i) hexagons (f/2); (ii) kinks (phase jumps of π) separating distinct flat domains; (iii) squares or stripes oscillating at f/4; (iv) hexagons (f/4); and (v) patterns disordered in both space and time. These different regimes are quite reproducible and the transitions between them are well defined.

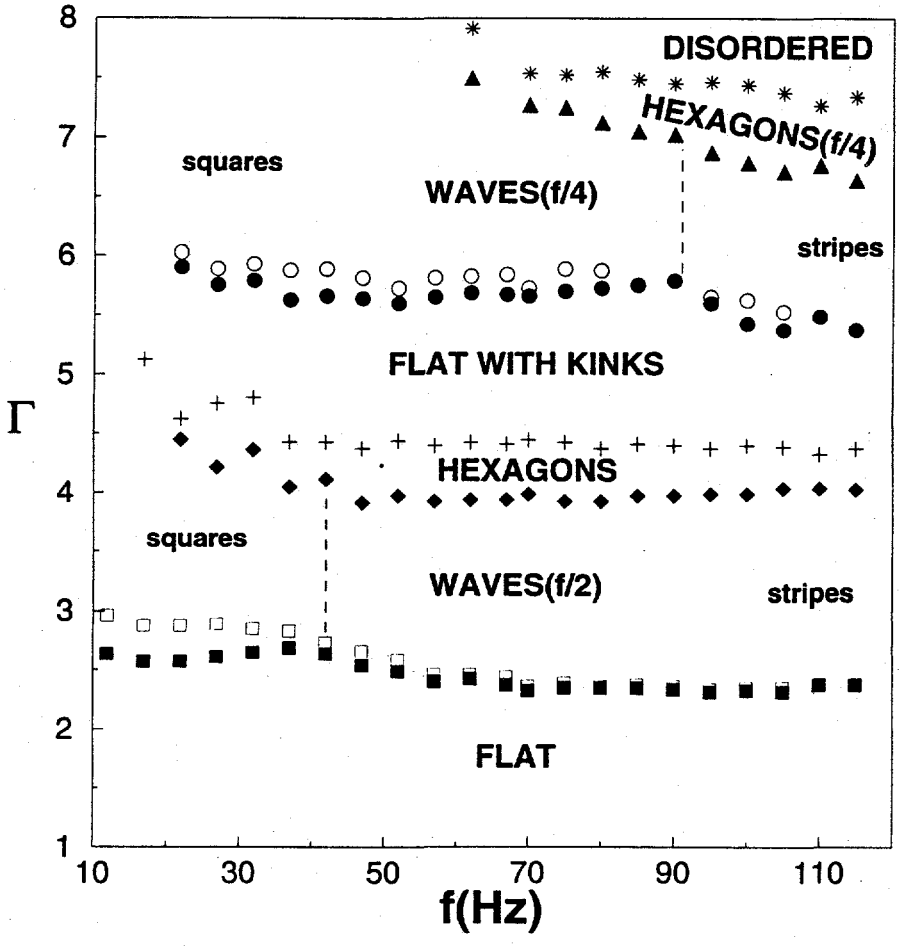

Fig. 4. Stability diagram showing different regimes in a granular layer (cf. Fig. 3) [17]. The transitions to squares (at frequency f/2 and f/4) are hysteretic, as indicated, while no hysteresis was measurable for the other transitions. The vertical dashed lines show the approximate center of the continuous transitions between squares and stripes.

Model

A one-dimensional model with a completely inelastic ball colliding with a sinusoidally oscillating platform indicates that the transitions from squares or stripes to hexagons and kinks are related to a period doubling bifurcation [17]. The model also provides insight into the higher bifurcations, even though of course the one-dimensional model cannot describe the form of the two-dimensional spatial patterns.

One goal of our study is to characterize and understand mixing in vibrated beds. Transport properties will be determined in the experiments by direct tracking of many particles, a technique that we have used in studying transport in quasi-geostrophic (oceanic-type) fluid flows [18]. The measurements will be compared with transport properties computed for two-dimensional models. This investigation should suggest ways in which the mixing properties of vibrated beds can be enhanced.

DISCUSSION

Our experiments have revealed new types of spatiotemporal patterns in reaction-diffusion systems and vibrated shallow granular beds. A fundamental understanding of the pattern forming processes in these systems should provide a stepping stone toward more efficient and innovative utilization of reaction-diffusion processes and vibrated beds.

ACKNOWLEDGEMENT

We gratefully acknowledge the participation of Qi Ouyang in some aspects of this research. This work was performed under the auspices of the U.S. Department of Energy Office of Basic Energy Sciences.

REFERENCES

1. R. D. VIGIL, Q. OUYANG, and H. L. SWINNEY, "Spatial variation of a short-lived intermediate chemical species in a Couette reactor," *J. Chem. Phys.* 96, 6126 (1992).

2. Q. OUYANG, H. L. SWINNEY, J. C. ROUX, P. DE KEPPER, and J. BOISSONADE, "Recovery of short-lived species in a Couette flow reactor," *AIChE J.* 38, 509 (1992).

3. B. THOMAS, M. O. MASON, Y. A. LIU, and A. M. SQUIRES, "Identifying states in shallow vibrated layers," *Powder Tech.* 57, 267 (1989).

4. B. J. ENNIS, J. GREEN, and R. DAVIES, "Particle Technology: the legacy of neglect in the U. S.," *Chem. Eng. Prog.* 90, 32 (1994).

5. Q. OUYANG and H. L. SWINNEY, "Transition from a uniform state to hexagonal and striped Turing patterns," *Nature* 352, 610 (1991).

6. Q. OUYANG, R. LI, G. LI, AND H. L. SWINNEY, "Dependence of Turing pattern wavelength on diffusion rate," *J. Chem. Phys.* 102, 2551 (1995).

7. Q. OUYANG and H. L. SWINNEY, "Onset and beyond Turing pattern formation," in *Chemical Waves and Patterns*, ed. by R. Kapral and K. Showalter, Kluwer Academic Publishers (1995), p. 269.

8. G. H. GUNARATNE, Q. OUYANG, and H. L. SWINNEY, "Pattern formation in the presence of symmetries," *Phys. Rev. E* 50, 2802 (1994).

9. K. J. LEE, W. D. McCORMICK, Q. OUYANG, and H. L. SWINNEY, "Pattern formation by interacting chemical fronts," *Science* 261, 192 (1993).

10. K. J. LEE and H. L. SWINNEY, "Lamellar structures and self-replicating spots in a reaction-diffusion system," *Phys. Rev. E* 51, 1899 (1995).

11. K. J. LEE, W. D. McCORMICK, J. E. PEARSON, and H. L. SWINNEY, "Experimental observation of self-replicating spots in a reaction-diffusion system," *Nature* 369, 215 (1994).

12. Q. OUYANG and H. L. SWINNEY, "Transition to chemical turbulence," *Chaos* 1, 411 (1991).

13. J. E. PEARSON, "Complex patterns in a simple system," *Science* 261, 189 (1993).

14. H. M. JAEGER, J. B. KNIGHT, C. H. LIU, and S. R. NAGEL, "What is shaking in the sandbox?," *MRS Bulletin* 19 (no. 5), 25 (1994).

15. H. K. PAK, E. VAN DOORN, AND R. P. BEHRINGER, "Effects of ambient gases on granular materials under vertical vibration," *Phys. Rev. Lett.*, to appear.

16. F. MELO, P. UMBANHOWAR, and H. L. SWINNEY, "Transition to parametric wave patterns in a vertically oscillated granular layer," *Phys. Rev. Lett.* 72, 172 (1994).

17. F. MELO, P. UMBANHOWAR, and H. L. SWINNEY, "Hexagons, kinks, and disordered patterns in a vertically oscillated granular layer," *to be published.*

18. T. H. SOLOMON, E. R. WEEKS, and H. L. SWINNEY, "Chaotic advection in a two-dimensional flow," *Physica D* 76, 70 (1995).

DEFORMATION AND CRACK GROWTH RESPONSE UNDER CYCLIC CREEP CONDITIONS

Frederick W. Brust, Jr.

Battelle Memorial Institute
Columbus, Ohio 43201, U.S.A.

ABSTRACT

To increase energy efficiency, new plants must operate at higher and higher temperatures. Moreover, power generation equipment continues to age and is being used far beyond its intended original design life. Some recent failures which unfortunately occurred with serious consequences have clearly illustrated that current methods for insuring safety and reliability of high temperature equipment is inadequate. Because of these concerns, an understanding of the high-temperature crack growth process is very important and has led to the following studies of the high temperature failure process.

This effort summarizes the results of some recent studies which investigate the phenomenon of high temperature creep fatigue crack growth. Experimental results which detail the process of creep fatigue, analytical studies which investigate why current methods are ineffective, and finally, a new approach which is based on the T*-integral and its ability to characterize the creep-fatigue crack growth process are discussed. The potential validity of this new predictive methodology is illustrated.

INTRODUCTION

As noted by Prager [1], the executive director of the Materials Property Council (MPC), historically equipment became obsolete, and was replaced with new designs, before the potential creep fatigue failure time was reached. As a result, experience with creep failures under nominal

design conditions has been limited. Some recent failures of high energy steam pipes in fossil power plants (see Lundin, et al. [2,3]), which were highly publicized and occurred with serious consequences, have clearly illustrated that creep rupture failures must be prevented. From the MPC studies (References [1] to [3]) and field experience it is now known that current engineering methods to predict the life of components that operate in these severe environments are ineffective. The reasons these current methods are ineffective are briefly summarized in the following paragraphs. Thorough and detailed discussion is provided in References [4-16].

The methods currently used for predicting the life of components that must operate in an environment where creep and creep/fatigue damage may develop are an extension of methods developed to predict elastic-plastic fracture. For an elastic-plastic cracked body, assuming deformation theory plasticity can adequately characterize the straining, one may show that the strength of the asymptotic field may be characterized by a path independent integral (the J-integral). Today, elastic plastic fracture is characterized in practice using J-integral tearing theory. It was quickly recognized that a creep analogue to plasticity using a Norton Creep Law (instead of deformation plasticity) leads to a path independent rate integral, C^*-integral, which characterizes the strength of the creep crack field. Following the same reasoning as that developed for elastic-plastic fracture, as adapted for creep crack growth, a creep fracture methodology was developed. The reason that the creep fracture analogy fails while the plasticity fracture technique works well are now clear: *deformation theory plasticity can accurately characterize plastic deformation near the high stresses which develop near the crack tip while Norton creep cannot characterize the creep deformations near a crack tip in a creeping body.* Moreover, when cyclic loads occur, the current methods for predicting creep-fatigue lives, which are based on Miner's rule, completely break down. Rather than use the strength of the asymptotic field as the creep fracture parameter, which depends on the chosen constitutive law, we have developed an energy-based fracture parameter which is independent of the chosen constitutive law. This method is discussed later.

CYCLIC CREEP DAMAGE

Consider a cracked body which is loaded and held at the load at a temperature which causes creep deformation to occur. The bulk of the creep strains will develop at the crack tip and emanate outward from the tip as time proceeds. A "creep zone" has thus developed at the crack tip. If the load is then removed from the body, the elastic strains surrounding the creep zone are prevented from going to zero because the inelastic creep strains prevent the body from attaining its original configuration. Hence, a compressive zone is induced in the crack region. This compressive zone can be quite large in size (see References [8,12,13] for calculations which illustrate the size of this zone). Figure 1 illustrates this effect with a blow up of the region near a crack tip produced from a detailed analysis of a 9Cr-Mo steel which experienced numerous cycles (see Reference [12] for details). If the load is then held at a zero or a negative load (or at any load smaller than the original load), a compressive creep zone which also emanates from the crack tip, and also grows with time, will develop in this compressive stress zone. If the load is then increased (positively) again, tensile stresses develop at the crack tip, a tensile creep zone re-

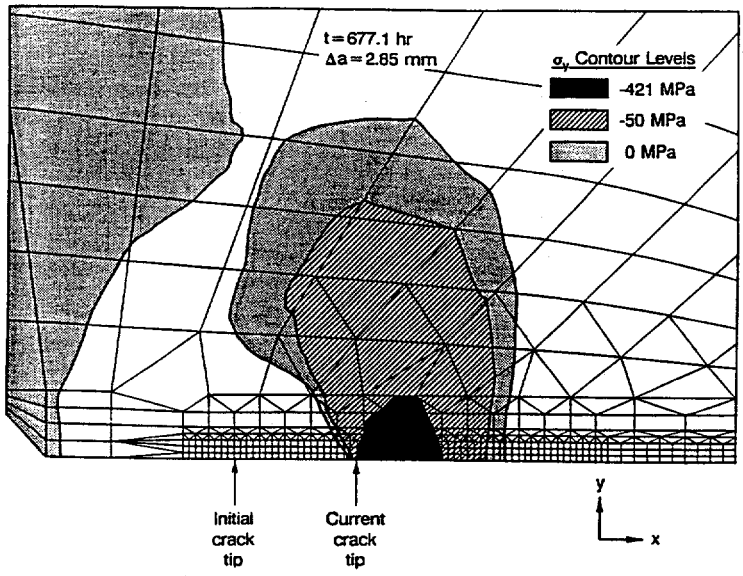

Figure 1. Contour Plots of the y-component of Stress at the End of an Unload/Hold Sequence forthe Analysis of a 9Cr-Mo Steel at 538 C. The Specimen Was Loaded and Held for 24 Hours, Unloaded and Held for 0.1 Hour, etc. The Results Shown Here are Near the End of the Test. Note the large size of the compressive stress zone even though the minimum load is zero.

develops, etc. It should be clear that, for any creep-fatigue situation where hold times occur, the crack tip region constantly experiences reversing tensile and compressive creep strains. Moreover, the creep strain rates which develop after each change in sign (ie., positive to negative or vice-versa) are greatly increased compared to the situation where no stress reversals occur [4,5]. This causes increased creep damage compared to the constant load case, and is the reason that classical creep fatigue crack growth methods break down.

EXPERIMENTAL OBSERVATIONS

The effect of the above described alternating tensile and compressive creep zones that develop near the crack tip during cyclic loading (even for R-ratios greater than zero) is increased creep damage and reduced life. A number of different tests were performed on 316 stainless steel at 650 C and 593 C, and on 9Cr-Mo steel at 538 C that illustrates this effect (see the cited References). Here we summarize some general trends.

Let us first examine some of the general conclusions which can be made regarding history-dependent loading in the time-dependent deformation regime. Figure 2 illustrates a load versus time sequence that was applied to one of the 9 Cr-Mo compact tension specimens at 538 C. An initial load period of 36 hours was made to ensure the development of an initial creep zone in the specimen. The unload hold times and subsequent reload times were continually decreased until about 90 hours, after which four-hour hold periods and one-hour unload periods were maintained until the specimen failed. This assured a truly variable load history.

An enlargement of the displacement versus time history for this experiment between 325

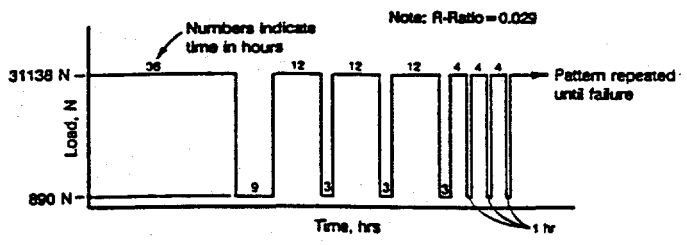

Figure 2. Load Time sequence (1st 9Cr-Mo test)

and 365 hours after beginning the test is illustrated in Figure 3. This specimen failed after about 400 hours. Another specimen was loaded to the same load level and was identical in all other ways to the above-described specimen except for a slightly larger initial crack. However, this specimen was held for 320 hours before unload/reload occurred, and only one cycle was applied. Figure 4 illustrates the displacement versus time history for this test. Note that this test failed at more than 600 hours.

Several important general conclusions can be drawn from these results:

- During the unload-hold period, load-point displacement recovery occurs. This is due to the compressive stresses which develop at the crack tip during unloading. The compressive stress zone size can be quite large, as was verified through computational studies, even though the global load is never less than zero.

- After reload, the displacement rates increase compared to the rates during the previous loading period. This is clearly seen in Figures 3 and 4. Note also that the displacement just after reloading is always smaller than the corresponding value just before unloading.

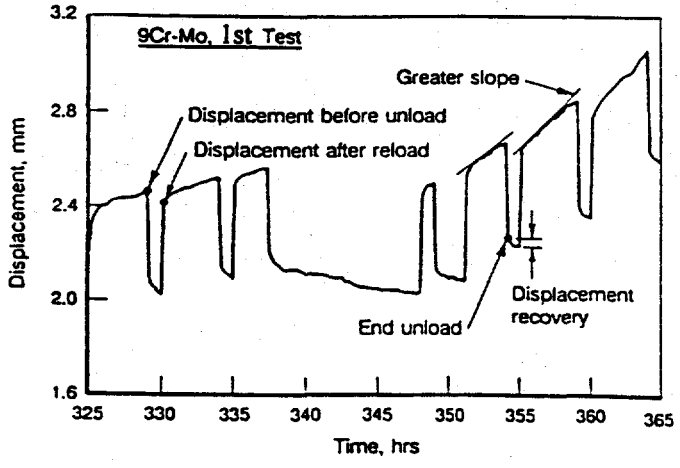

Figure 3. Displacement Time History 1st 9CrMo Test.

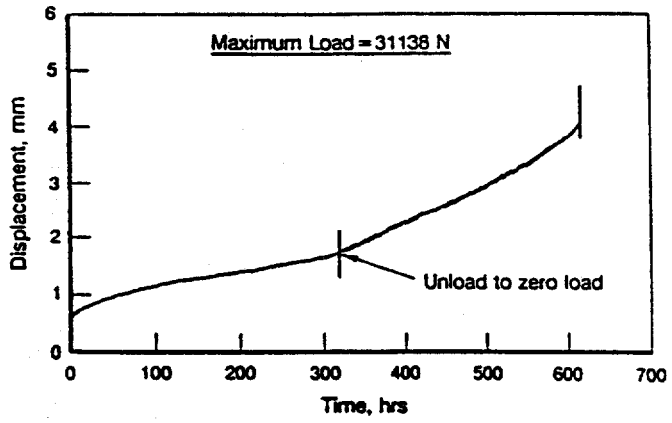

Figure 4. Displacement Time History - 2nd 9CrMo Test.

- Load-history effects significantly decrease life compared to the nearly constant load (only one unload) test, i.e., in this case the constant load test lasted nearly 1.5 times longer.

ANALYSIS SUMMARY

Here we briefly show results of an asymptotic study before showing results from an analysis of an experiment. Consider a stationary crack subjected to the following load sequence: (i) Load with 24-hour hold period, (ii) unload (to zero load) and hold for one hour, (iii) reload and hold for 24 hours, (iv) etc. This means that the end of the load-hold periods were 24, 49, 74, and 99 hours. An extremely refined symmetric finite element mesh was developed with 10 rings of six-noded isoparametric triangular elements surrounding the crack tip and eight-noded elements elsewhere with the crack-tip element size equal to .0005 times the uncracked ligament. This refinement is about 2.5 times more refined compared with the classical HRR field studies of Shih and German. A classical strain-hardening (S-H) and the Murakami-Ohno (M-O) cyclic creep law were used to model the problem. Creep properties for 9 Cr-Mo steel were used. Figure 4 illustrates the theta component (i.e., perpendicular to the crack) of creep strain as a function of the distance, R, ahead of, and parallel to, the crack. Note that the creep strain as calculated using the M-O law continuously drifts away from the strains evaluated using a classical law. This is because the creep strain rates after a *change in stress direction* which occurs near the crack during global load changes become very large. This is observed both experimentally and predicted using M-O. The S-H law cannot capture this effect. The importance of this is that the true deformation response of the cracked body must be accounted for in order to adequately predict the damage accumulation near the crack. Examination of stresses also reveals that the strength of the asymptotic field also changes from cycle to cycle. We thus conclude that current engineering methods, which are based on correlating creep-crack growth rates to the strength of an asymptotic field assuming a classical creep law (and constant load conditions), are not valid for variable load conditions.

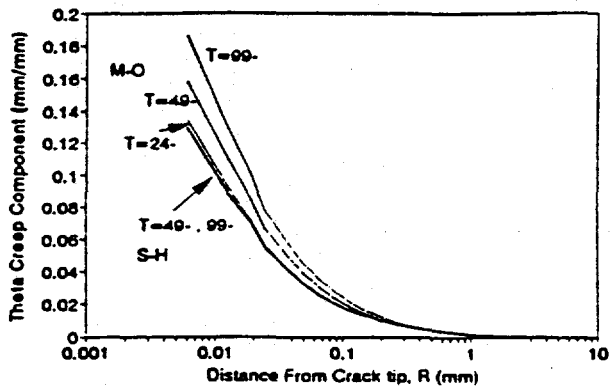

Figure 5 Asymptotic Creep Strains.

Finally, the analysis results of one of the 9 Cr-Mo tests (i.e., third test) are presented. This specimen had a load sequence consisting of (i) load and hold for 24 hours, (ii) unload and hold for 5 minutes, (iii) reload and hold for 24 hours, etc., (i.e., different from Figure 1 and 3). The maximum load was 23.353 KN, and the minimum load was zero.

The finite element model was forced to follow the load-time and crack-growth history. The constitutive law used to perform the analyses is based on the work of Murakami and Ohno. The numerical implementation of this law and the finite element model is detailed in References [7,13]. An implicit numerical scheme is used, crack growth is modeled in the two dimensional problems using a node release technique, and the T*-integral is evaluated using a direct approach. Other integral parameters are also evaluated. T* can be shown to represent the energy release rate to a process zone near the growing crack tip per unit crack growth. Reference [16] details the theory of T* as well as providing a number of verification examples for different conditions.

Load-line displacements were predicted as well as a number of integral fracture parameters. The fracture parameters considered here are integral parameters, which have an energetic physical interpretation. The T^*, J_W (Watanabe), J_M (McClintock), $\hat{J}$ (Aoki, et al.), and J_B (Blackburn) integrals were evaluated throughout the history (please see references for detailed discussions of these parameters). The crack initiated at about 192 hours and failure occurred after 700 hours in the test. Note that the entire load history was modeled.

Figure 6 shows a comparison of the maximum displacements (at the end of the load-hold period) and minimum displacements (at the end of the unload-hold periods). It is seen that the predicted displacements compare quite well with the experimental results, which suggests that the model is adequate. The predicted displacements begin to accelerate upward at about 600 hours while the experimental results begin to increase at about 650 hours, i.e., the analysis predictions are a little conservative here. The displacement trends of displacement recovery after unload, and displacement rates increasing after reload (of the type illustrated in Figure 3) were also predicted reasonably well compared to the data.

Figure 7 compares all of the integral parameters as a function of time. As indicated in Figure 7, crack growth begins at about 192 hours, after the eighth unloading. Note that, before crack growth, all of the integrals experience a step jump after a load cycle indicating that variable loads increase creep damage conditions as measured by these parameters. Note that the T^* and

J_W integrals attain a nearly constant value during the crack-growth phase (observe the horizontal lines in Figure 7). This result suggests that a constant value of T^* or J_W can characterize crack growth under creep fatigue conditions. Moreover, crack initiation can be predicted. At about 628 hours the integral parameters become unstable, suggesting that crack instability is predicted. The analysis results of the other tests also showed this same performance of the integral parameters. Energetic parameters can characterize load history dependent fracture while asymptotic methods must be abandoned.

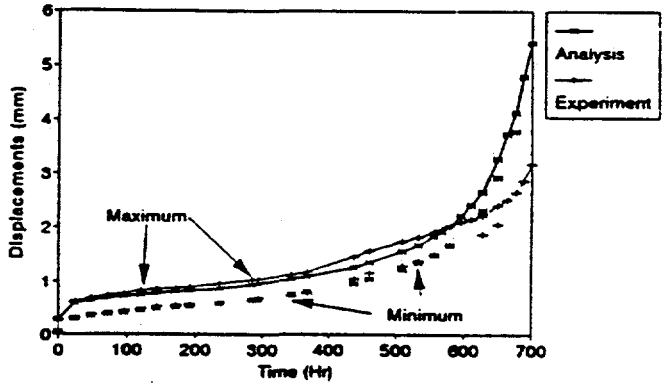

Figure 6. Displacement Comparisons for 3rd 9Cr-Mo test.

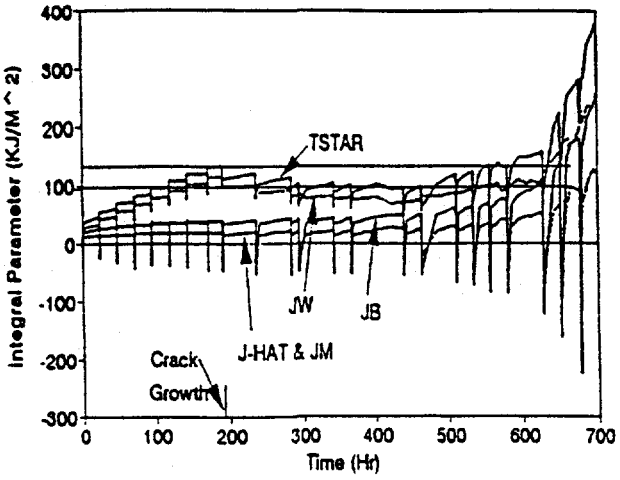

Figure 7. Behavior of Integral Parameters for 3rd 9Cr-Mo Test.

ACKNOWLEDGEMENTS

This work was performed under the auspices of the U.S. Department of Energy, Office of Basic Engineering Science. The authors thank Drs. O. Manley and James Welty for their support.

REFERENCES

1. M. PRAGER, "Issues in Life Assessment of Chrome-Moly Welds", *ASME PVP-Vol. 2391,* MPC-Vol. 33 (1992).

2. C. D. LUNDIN ET. AL., "Failure Analysis of a Service-Exposed Hot Reheat Steam Line in a Utility Steam Plant", Excerpt from WRC Bulletin 354, June (1990).

3. C. D. LUNDIN AND Y. WANG, "Repair Welding of Service Exposed Cr-Mo Steel Weldments", Excerpt from WRC Bulletin 348, November (1989).

4. P. KRISHNASWAMY, F. W. BRUST, AND N. D. GHADIALI, "A Finite Element Algorithm To Study Creep Crack Growth Based on the Creep Hardening Surface", *Int. J. Num. Meth. Eng.* 38 (6), 969-988 (1995).

5. F. W. BRUST, P. KRISHNASWAMY, AND B. S. MAJUMDAR, "Consideration of History Dependent Damage in Creep Crack Growth", *Proc. 10th Symp. Energy Eng. Sci.,* Argonne, Ill., May (1992).

6. P. KRISHNASWAMY, F. W. BRUST, AND N. D. GHADIALI, "Finite Element Analysis of History Dependent Damage in Time Dependent Fracture Mechanics", *ASME J. Pres. Ves. Tech.,* (115), 339-347 (1993).

7. F. W. BRUST AND P. KRISHNASWAMY, "A Computational Study of the Time Dependent Crack Growth Process", *ASME AD-Vol 27,* ed. A. Nagar (1992).

8. F. W. BRUST AND B. S. MAJUMDAR," Load History Effects on Creep Crack Growth", *Eng. Fract. Mech.,* 49 (6), 809-837 (1994).

9. F. W. BRUST AND B. S. MAJUMDAR, "Studies of Creep Crack Growth Under History Dependent Loading", *Proc. ICF-8,* Ukraine, June (1993). Also to Appear *J. Matl. Sci.*

10. F. W. BRUST, P. KRISHNASWAMY, AND B. S. MAJUMDAR, "Further Studies of History Dependent Loading in the Creep-Crack Growth Regime", in Fracture Mech. - Applications and New Matls., ed. A. Mehta, *ASME PVP Vol. 260,* July (1993).

11. P. KRISHNASWAMY AND F. W. BRUST, "Finite Element Modeling of Creep Crack Growth In 316 Stainless and 9 Cr-Mo Steels", *Proc. 11th Int. Invit. Symp. On the Unif. Of Anal., Comp., Sol. Meth.,* Boston, MA, August (1993).

12. F. W. BRUST, "Investigations of High Temperature Damage and Crack Growth Under Variable Load Histories", *Int. J. Sol. Structs.*, in press (1995).

13. F. W. BRUST, "Numerical Modeling and Experiments of Creep Crack Growth Under Cyclic Loading", *ASTM STP 1256,* (1995).

14. F. W. BRUST, "The Effects of Load History on Creep Damage Evolution", *ASME PVP Volume,* July (1995).

15. F. W. BRUST, "An Investigation of the Effects of History Dependent Damage in Time Dependent Fracture Mechanics", *To Appear Proc. ICES-95,* August (1995).

16. F. W. BRUST, "The T*-Integral: Definition and Use for Predicting Damage Accumulation and Fracture", invited pres. at *A. C. Eringen Medal of the Soc. Of Eng. Sci. Award*, New Orleans. Also to appear in *Recent Advances in Engineering Science,* November (1995).

ADVANCED LASER DIAGNOSTICS FOR DIAMOND DEPOSITION RESEARCH

C.H. Kruger, T.G. Owano, E.H. Wahl

High Temperature Gasdynamics Laboratory
Department of Mechanical Engineering
Stanford University
Stanford, CA 94305-3032

ABSTRACT

Chemical Vapor Deposition (CVD) using thermal plasmas is attractive for diamond synthesis applications due to the inherently high reactant densities and throughput, but the associated high gas-phase collision rates in the boundary layer above the substrate produce steep thermal and species gradients which can drive the complex plasma chemistry away from optimal conditions. To understand and control these environments, accurate measurements of temperature and species concentrations within the reacting boundary layer are needed. This is challenging in atmospheric pressure reactors due to the highly luminous environment, steep thermal and species gradients, and small spatial scales. The applicability of degenerate four-wave mixing (DFWM) as a spectroscopic probe of atmospheric pressure reacting plasmas has been investigated. This powerful, nonlinear technique has been applied to the measurement of temperature and radical species concentrations in the boundary layer of a diamond growth substrate immersed in a flowing atmospheric pressure plasma. In-situ measurements of CH and C_2 radicals have been performed to determine spatially resolved profiles of vibrational temperature, rotational temperature, and species concentration. Results of these measurements are compared with the predictions of a detailed numerical simulation.

INTRODUCTION

Thermal plasma CVD of diamond thin films is an attractive synthesis technique due to several inherent attributes. The high reactant densities available at atmospheric pressure can produce high radical fluxes to the deposition surface, resulting in high growth rates. Operation at atmospheric pressure also precludes the loading and unloading of samples to be coated from a vacuum system, yielding a corresponding decrease in process cost and complexity. From a modeling standpoint, the atmospheric pressure reacting flowfield is in the continuum, rather than the molecular or transitional flow regime and is more readily simulated. These beneficial attributes of atmospheric pressure deposition are tempered by the presence of a collision dominated, chemically reacting boundary layer above the substrate surface in which important

chemical species are both rapidly produced and destroyed. This aspect of atmospheric pressure techniques is strikingly different from low pressure deposition techniques in which production and diffusion of chemical species controls the deposition process

Previous studies of the atmospheric pressure deposition environment have yielded important knowledge of the parameters affecting diamond formation,[1-4] but have been limited to mostly post-deposition characterizations and comparisons. To further explore the nature of the atmospheric pressure diamond deposition environment and process, it is necessary to make accurate in-situ measurements of temperatures and species concentrations within the thin (< 1 cm) reacting boundary layer over the substrate, and compare these fundamental quantities with detailed simulations.

It is quite difficult, for many diagnostic techniques, to provide useful and accurate information from such a harsh and potentially nonequilibrium environment. Sensitive measurement of temperature and trace radical concentrations within a reacting boundary layer is a challenging problem in atmospheric pressure reactors due to the highly luminous environment, small spatial scales, and steep thermal and concentration gradients. It is in this environment where the application of sensitive, laser based diagnostic techniques can allow the detailed measurement of temperature and trace radical concentrations to be made, and compared to models of the deposition environment. The application of a powerful non-linear laser spectroscopy, degenerate four wave mixing (DFWM), as a gas-phase optical diagnostic has opened the door for significant advancement in the area of atmospheric pressure plasma chemistry, since it can provide high sensitivity and spatial resolution with a coherent, phase conjugate signal which can be readily discriminated against the plasma luminosity.[5-8]

The DFWM technique utilizes three laser beams of a single wavelength interacting with the plasma to produce a fourth spatially coherent, polarized signal beam that can be collected with high efficiency, and effectively filtered from the intense plasma luminosity. This feature is perhaps the greatest advantage of DFWM over other traditional diagnostic tools of atmospheric pressure plasmas which are often disabled or corrupted by the intense background luminosity. DFWM is found to be an extremely useful nonintrusive probe of the plasma, capable of providing high spectral and spatial resolution, and permitting measurements of temperature and relative species concentrations of trace radicals under conditions in which other spectroscopic techniques fail. Since DFWM can be used to probe the ground state of electronic transitions, it is much less subject to misinterpretation as a result of nonequilibrium effects[9] than conventional techniques such as optical emission spectroscopy (OES). Measurements of vibrational and rotational temperatures, as well as relative concentration profiles for CH and C_2 radicals have been measured in the thin boundary layer of a diamond-growth substrate immersed in a flowing atmospheric pressure plasma. DFWM measurements of temperature and relative species concentrations are compared with the results of a detailed numerical simulation[10] of the reacting plasma, and found to be in agreement.

EXPERIMENTAL FACILITY

The RF inductively coupled plasma (ICP) torch facility has been described in previous work.[1,4] The present experiments were conducted inside a water cooled quartz test section which is shown in schematic cut-away along with the plasma torch head in Figure 1. Open-ended laser access ports, approximately 6.5 cm downstream of the nozzle exit, enable the DFWM pump and

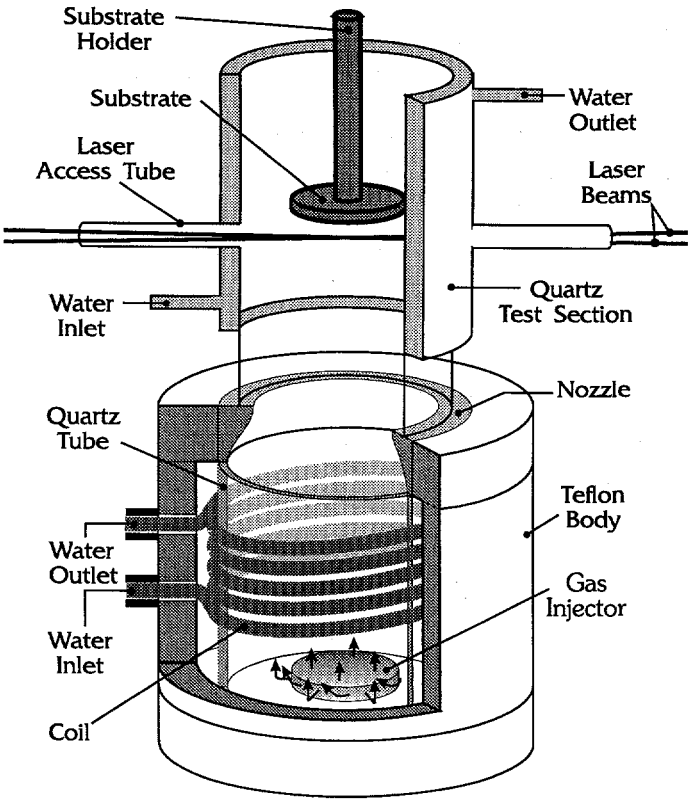

Figure 1. Schematic of RF-ICP reactor.

probe beams to enter and exit the reactor unhindered, and to cross at a location directly below the stagnation point of the substrate. Substrates are supported within the quartz test section in a stagnation point flow geometry by means of a water cooled holder. The substrate can be vertically translated in-situ to allow laser measurements to be made at various points through the boundary layer. Substrate temperature is monitored with a Minolta/Land Cyclops 152 infra-red optical pyrometer. Reactant gases (hydrogen and methane) are premixed with the carrier gas (argon) before passage through the RF discharge.

The optical configuration for this facility is shown schematically in Figure 2.. Laser beams for the DFWM experiments are produced using a Nd:YAG pumped dye laser system (~0.05 cm^{-1} bandwidth). The output of the laser is spatially filtered to improve beam quality, and reduced in intensity with a variably rotated half-wave plate, fixed polarizer combination. The beam is then split into three beams (of approximately equal energy at the test section), the backward pump beam (denoted E_b), the probe beam (denoted E_p), and the forward pump beam (denoted E_f). Polarization of the backward pump beam is rotated with a half-wave plate to be perpendicular to the polarization of the forward pump and probe beams, thus aiding signal isolation. Beam convergence is adjusted to produce a mild focus at the mid-line of the test section, producing beam waists of approximately 300 μm diameter. The forward and backward pump beams are brought coaxial and counterpropagating through the test section laser ports, and the probe beam crosses the pump beams at a slight angle (≈2.1°) directly beneath the stagnation region of the

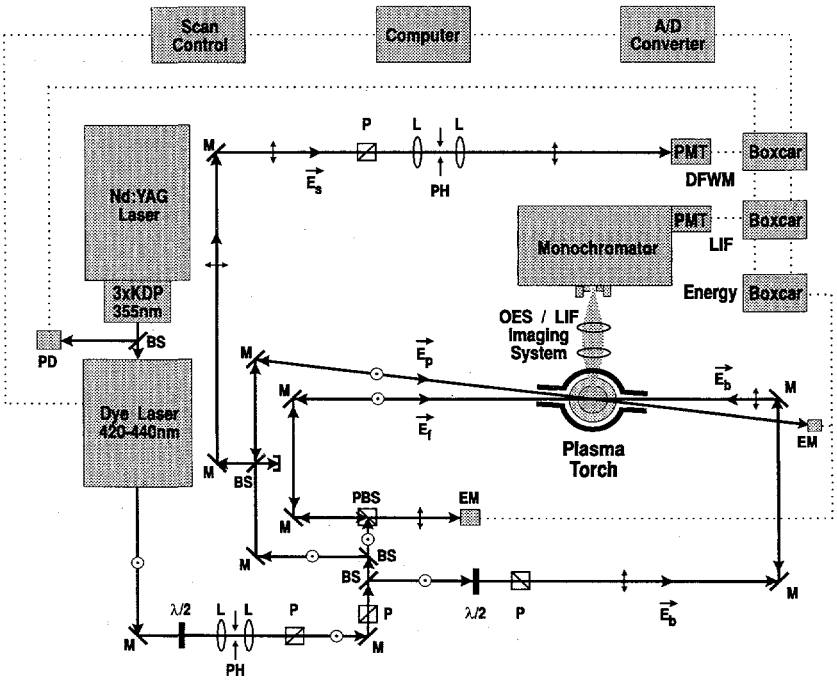

Figure 2. Schematic of optical configuration.

substrate. The three beams lie in a plane parallel to the substrate surface. Geometric interaction length of the pump and probe beams is approximately 16 mm (parallel to the substrate surface).

The phase-conjugate signal beam (denoted E_S) is generated within the interaction region and follows the reverse path of the probe beam out of the test section. This signal beam counterpropagating along the probe beam line is separated by means of a beamsplitter, spatially filtered to reject incoherent scattering, and detected with an unfiltered photomultiplier tube (Hamamatsu Model R212). Beam energy is continuously monitored by means of two joulemeters (Molectron J4-09) which terminate the probe and backward pump beams.

DEGENERATE FOUR-WAVE MIXING RESULTS

The applicability of in-situ DFWM to the atmospheric pressure diamond synthesis environment has been investigated using the well controlled, atmospheric pressure ICP reactor (Figure 1). It was desired to make in-situ measurements during normal operation of the atmospheric pressure RF-ICP diamond synthesis reactor - with a substrate in place, and growing diamond. The conditions chosen for these studies were indeed diamond growth conditions (although they were not optimized for best possible growth) and all measurements reported here were taken with the growing substrate in place. The reactor gas feed mixture was comprised of 106.5 l/min Ar, 12.0 l/min H_2, and 0.8% to 10% CH_4 (in H_2) premixed before introduction to the plasma torch. Calorimetric energy balance of the reactor indicates a net plasma enthalpy of 6 kW leaving the nozzle exit. The molybdenum substrate had a measured surface temperature of 1035°C.

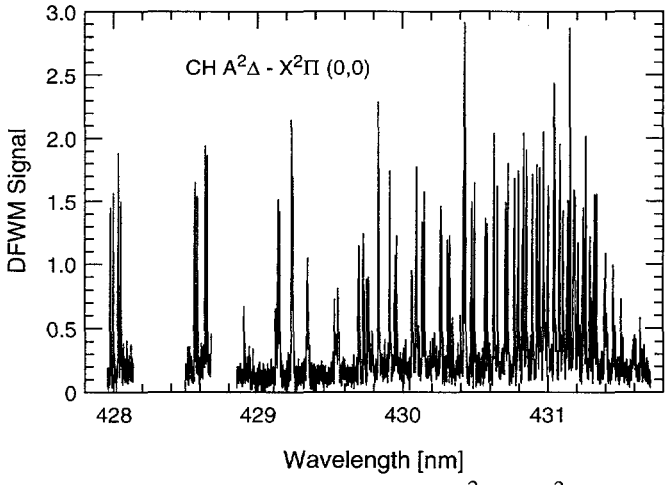

Figure 3. DFWM Spectra of CH $A^2\Delta \leftarrow X^2\Pi$ (0,0)

The CH radical was probed with in-situ DFWM measurements of the CH $A^2\Delta \leftarrow X^2\Pi$ (0,0) system near 431 nm. Figure 3 shows a DFWM spectrum of this region taken with approximately 10 μJ laser beam energies. The small groups of lines to the left side of Figure 3 are the grouped components of individual rotational lines in the R branch, while the closely spaced lines toward the right side of the figure are individual lines comprising the Q branch (the P branch is not shown). The v″=0 and v″=1 sets of individual R branch lines are closely grouped (Figure 4) and permit determination of vibrational temperatures. The Q branch region allows fairly rapid measurements of several v=0 lines, thus permitting rotational temperature measurements to be made throughout the

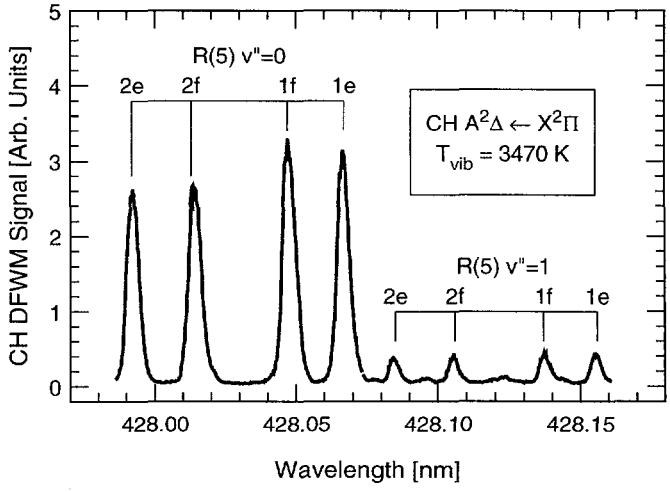

Figure 4. CH R(5) v"=0 and v"=1 components.

reacting boundary layer. An example of this rotational temperature determination is shown in Figure 5 where the intensity of measured Q branch lines (from N = 6 to 20) are plotted on a DFWM Boltzmann plot. This yields a straight line distribution (indicating rotational equilibration) corresponding to a rotational temperature of 3135 K. The C_2 radical was probed with in situ DFWM measurements of the C_2 $d^3\Pi_g \leftarrow a^3\Pi_u$ (3,1) system near 437 nm.

A stoichiometric study of the freestream concentrations of CH and C_2 radicals as a function of methane to hydrogen feed gas ratio was performed to address several questions. First, since the methane to hydrogen feed gas ratio is an important process parameter in controlling quality of the deposited diamond, it was of interest to determine the sensitivity of DFWM measurements of CH and C_2 radicals to this ratio. Secondly, an important assumption in modeling this environment[4-7,10] is that the freestream be a known input condition; more specifically that the freestream plasma is in chemical equilibrium at the measured freestream temperature. Although this a priori assumption is quite reasonable since the flowtime of the plasma from the region of excitation is chemically very long (10 ms compared to a chemical relaxation time of approximately 1 ms), it is nonetheless a prudent idea to test its validity for these trace radicals.

In Figure 6, the results of this stoichiometric study are shown for methane to hydrogen feed gas ratios ranging from approximately 0.8% to 10%, with measured freestream temperature constant at 3500 K. The closed and open circles correspond to the CH and C_2 relative mole fractions measured using DFWM, and the solid lines represent equilibrium chemical composition for the plasma mixture at 3500 K. (The CH and C_2 DFWM relative concentration data sets have been normalized to the equilibrium composition lines for comparison). The agreement between the equilibrium calculation and the measured relative mole fractions of CH and C_2 as a function of methane to hydrogen feed gas ratio is a very good indication that the freestream is indeed in chemical equilibrium.

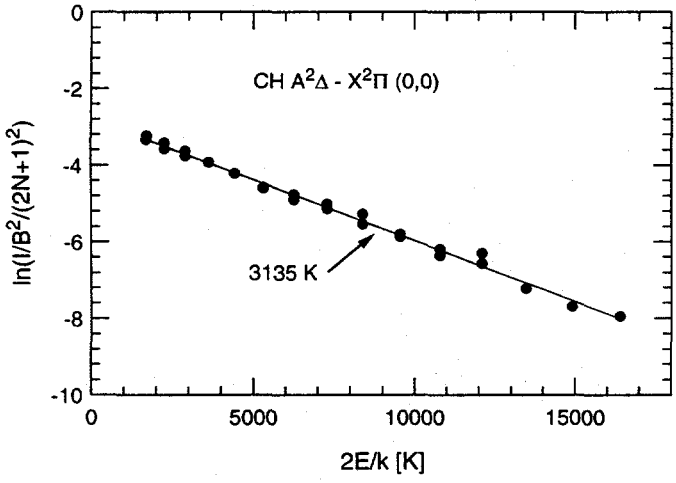

Figure 5. DFWM rotational Boltzmann plot

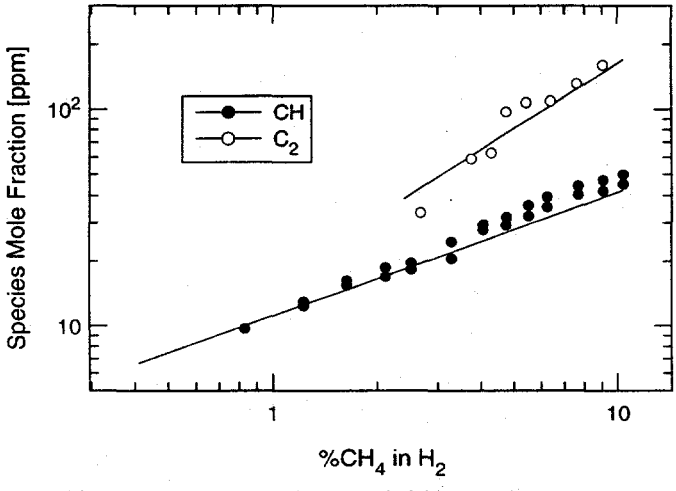

Figure 6. Freestream stoichiometric study.

Temperature and concentration profiles within the reacting boundary layer itself were also probed using DFWM. A comparison of measured CH vibrational and rotational temperatures along the stagnation line of the substrate with values from the computational simulation is shown in Figure 7. Boundary conditions for the simulation are the measured freestream temperature of 3900 K, an estimated freestream velocity of 8 m/s, and the measured substrate temperature of 1035°C. We can see in

Figure 7 the predicted thermal boundary layer (≈6mm thick) with a steep fall off in temperature very close to the substrate. The measured CH vibrational temperatures are in close agreement with the predictions, although the loss in signal of the v=1 transitions in the cooler region very near the substrate prevents accurate vibrational temperature measurement for distances < 2mm. Rotational temperatures measurements from the CH v=0 lines, which remain strong enough for accurate measurement closer to the substrate are in good agreement with both the measured vibrational temperatures and the computational simulation. It is possible to make rotational temperature measurements even closer to the substrate than shown in Figure 7, but for these experimental conditions the CH concentration in that region has dropped below approximately 2 ppm, which is our current detection limit.

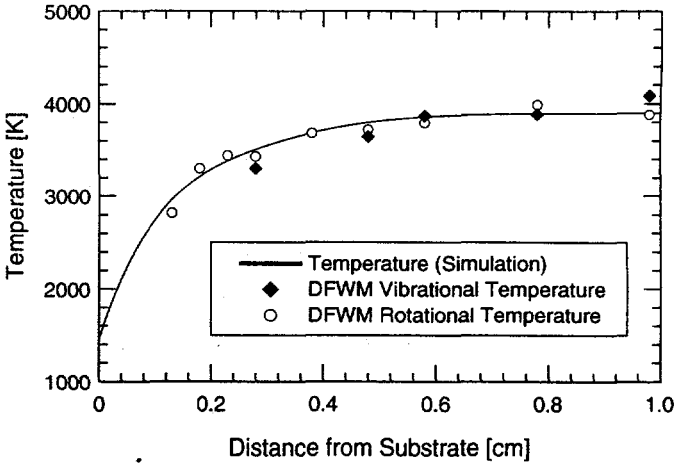

Figure 7. Boundary layer temperature profiles.

Measurements of the relative CH and C_2 mole fractions within the substrate boundary layer are compared to results of the computational simulation in Figures 8 and 9. In Figure 8, the CH mole fraction is approximately 20 ppm in the freestream (4100 K) and is predicted to first rise within the approximately 6 mm thick boundary layer (due to production) as the plasma cools toward approximately 3700 K, reaching a peak of approximately 55 ppm at 2 mm from the substrate surface, then to be destroyed as the plasma cools further on its approach to the substrate surface. In Figure 9, we see a similar behavior for the C_2 concentration profile with a much higher peak concentration (~300 ppm). We can see that the DFWM measurements of relative CH and C_2 mole fraction (which have been scaled to the peak of the predicted curve, and are in agreement with the calibrated equilibrium freestream) correspond closely to the predicted concentration in both trend and magnitude, accurately reflecting the production and destruction of the radicals within the boundary layer and demonstrating the ability of DFWM to probe this small, harsh reaction zone.

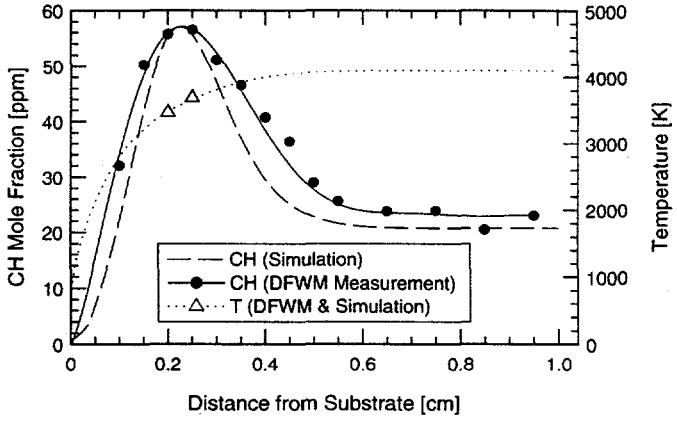

Figure 8. CH concentration profile.

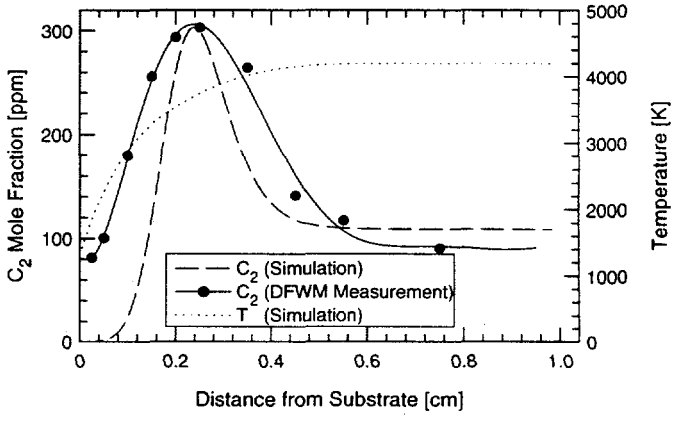

Figure 9. C_2 concentration profile.

CAVITY RING-DOWN SPECTROSCOPY RESULTS

Cavity ring-down spectroscopy is another emerging technique that also offers extremely sensitive, spatially resolved information from plasma environments via cavity-coupled laser absorption. By measuring the ring-down time of a laser pulse injected into an optical cavity which surrounds the plasma of interest, CRDS enables a very sensitive, absolute determination of the line-of-sight absorptivity of the plasma. Since this technique measures the ring-down time of the cavity, rather than the fractional absorbance ($I_{transmitted}/I_{incident}$), the measurement becomes insensitive to the intensity if the incident pulse which can be a major source of uncertainty in ordinary absorption (and multi-pass absorption) techniques. In this manner, plasma absorbance as small as one part in 10^5 (per cavity round-trip) can be accurately measured, thus yielding very sensitive measurements of absolute species concentrations.

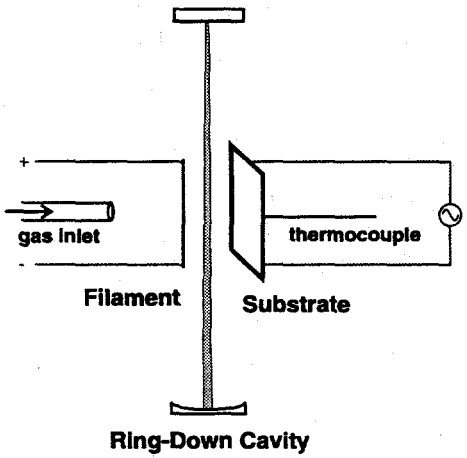

Figure 10. Schematic of CRDS system.

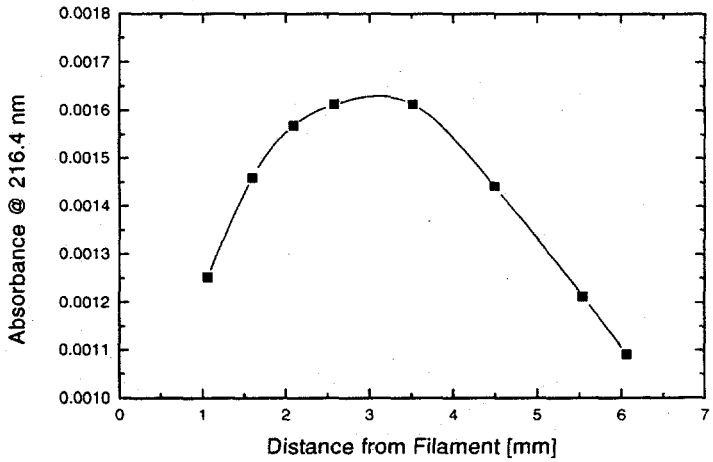

Figure 11. Spatial profile of methyl absorbance.

In the past year, we have been successful in applying cavity ring-down spectroscopy to the measurement of absolute concentration of methyl radicals in a hot filament reactor. The experimental schematic of these experiments is shown in Figure 10. Although this technique produces a line of sight averaged quantity, it provides high spatial resolution in the one spatial dimension of interest within this system, and more importantly provides absolute concentration measurements at single pass absorbances as low as $1x10^{-5}$. Using this technique, spatial profiles of methyl radical concentrations have been measured between the excitation filament and the deposition substrate, as a function of process variables such as flow direction, pressure, filament temperature, and substrate temperature. These preliminary investigations have provided evidence of the independence of flow direction within these reactors. CRDS measurements have also shown clear indications that for certain conditions, the methyl concentration peaks approximately 4 mm away from the filament surface, which is contrary to the currently accepted mechanism of methyl formation from excited hydrogen atoms close to the filament, but in agreement with more recent REMPI measurements of other investigators. A spatial distribution of methyl absorbance at 216.4 nm under typical hot-filamnet reactor operating conditions is shown in Figure 11. Many investigators are currently working to understand and model the complex plasma and surface chemistry within these systems, and CRDS appears to be a promising technique to experimentally validate those efforts.

CONCLUSIONS

Degenerate four-wave mixing has been demonstrated as a sensitive, spatially resolved diagnostic of boundary layer chemistry in thermal plasma CVD of diamond. The coherent, phase-conjugate signal produced in this technique enables the rejection of intense plasma luminosity, and allows the accurate interrogation of temperature and trace (ppm level) radical concentrations within the reacting plasma. In-situ measurements of vibrational and rotational temperatures, as well as relative CH and C_2 radical concentrations in the reacting boundary layer of a diamond growth substrate are found to be in good agreement with model predictions.

ACKNOWLEDGMENTS

The authors would like to acknowledge contributions by the companion research program of Prof. R.N. Zare, with Dr. P. Zalicki and Y. Ma (DOE Grant #DE-FG03-92ER14304)

REFERENCES

1. T.G. OWANO and C.H. KRUGER, "Parametric Study of Atmospheric-Pressure Diamond Synthesis with an Inductively Coupled Plasma Torch," *P. Chem. and P. Proc.* 13, 433 (1993).
2. B.W. WU and S.L. GIRSHICK, "Atomic Carbon Vapor as a Diamond Growth Precursor in Thermal Plasmas," *J. of Appl. Phys.* 75, 3914 (1993).
3. R. HERNBERG, T. LEPISTO, T. MANTYLA, T. STENBERG, and J. VATTULAINEN, "Diamond Film Synthesis on Mo in Thermal RF Plasma," *Diamond and Related Materials* **1** (1992) 255
4. S.K. BALDWIN, T.G. OWANO, and C.H. KRUGER, "Growth Rate Studies of CVD Diamond in an RF Plasma Torch," *P. Chem. and P. Proc.* 14, 383 (1994).
5. T.G. OWANO, C.H. KRUGER, D.S. GREEN, S. WILLIAMS, and R.N. ZARE, "Degenerate Four-Wave Mixing Diagnostics of Atmospheric Pressure Diamond Deposition," *Diamond and Related Materials* 2, 661 (1993).
6. D.S. GREEN, T.G. OWANO, S. WILLIAMS, D.G. GOODWIN, R.N. ZARE, and C.H. KRUGER, "Boundary Layer Profiles in Plasma Chemical Vapor Deposition," *Science* 259, 1726 (1993).
7. T.G. OWANO, E.H. WAHL, C.H. KRUGER, D.S. GREEN, and R.N. ZARE, "Degenerate Four-Wave Mixing as a Spectroscopic Probe of Atmospheric Pressure Reacting Plasmas," *Proceedings of the 11th International Symposium on Plasma Chemistry* 1, 416 (1993).
8. S. WILLIAMS, D.S. GREEN, S. SETHURAMAN, and R.N. ZARE, "Detection of Trace Species in Hostile Environments Using Degenerate Four-Wave Mixing: CH in an Atmospheric Pressure Flame," *J. Am. Chem. Soc.* 114, 9122 (1992).
9. C.H. KRUGER, M.H. GORDON, and T.G. OWANO, "Measurements of Nonequilibrium Effects in Thermal Plasmas," *J. of Pure and Appl. Chem.* 64, 637 (1992).
10) D.G. GOODWIN, and G.G. GAVILLET, "Numerical Modeling of the Filament-Assisted Diamond Growth Environment," *J. Appl. Phys.* 68, 6393 (1990).

Physical Models of Polarization Mode Dispersion

C. R. Menyuk and P. K. A. Wai

Department of Electrical Engineering, University of Maryland
Baltimore, MD 21228-5398

ABSTRACT

The effect of randomly varying birefringence on light propagation in optical fibers is studied theoretically in the parameter regime that will be used for long-distance communications. In this regime, the birefringence is large and varies very rapidly in comparison to the nonlinear and dispersive scale lengths. We determine the polarization mode dispersion, and we show that physically realistic models yield the same result for polarization mode dispersion as earlier heuristic models that were introduced by Poole. We also prove an ergodic theorem.

1. INTRODUCTION

There are two distinct data formats that are being actively studied for possible use in long-distance communication systems. The first data format uses solitons as 1-bits in the communication system. By balancing nonlinearity and dispersion, solitons avoid the bad effects that either phenomenon would lead to on its own. From a strict mathematical standpoint, the optical fiber does not support solitons—merely soliton-like pulses—because the equations that describe real-world fibers are not integrable. Nonetheless, the equations are closely related to the nonlinear Schrödinger equation, and there is ample theoretical and experimental evidence that solitons are robust in the sense that the soliton-like pulses that actually propagate in fibers have virtually all the properties of true solitons on the length scale over which experiments are done.[1] Soliton pulses are referred to in the vernacular of communication systems as RZ (return-to-zero) pulses. As shown in the top half of Fig. 1, the energy of the solitons is concentrated in the middle of the timing window, and the amplitude is always zero at the edge of the window. The second format is shown in the bottom half of Fig. 1 and is referred to as NRZ (non-return-to-zero). In this format, the

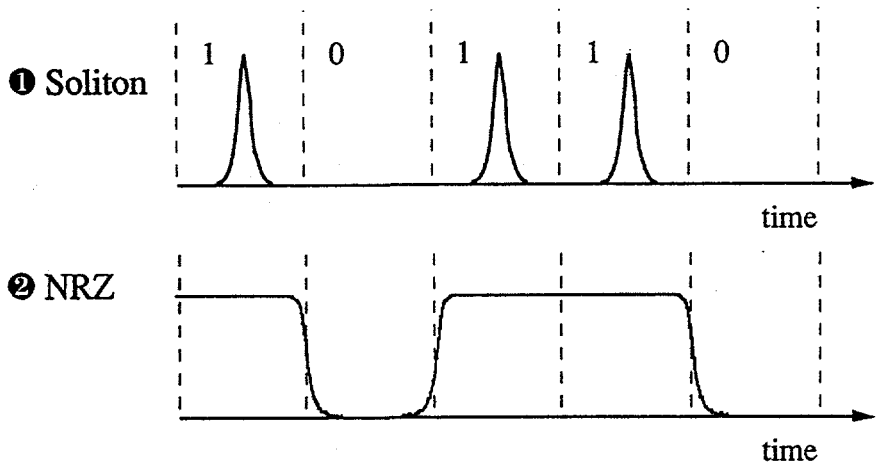

FIGURE 1. Intensity variation of a 10110 bit stream in both soliton and NRZ communications.

energy of a 1-bit is spread nearly evenly throughout the timing window. This format is the one that has been traditionally used in long-distance communications. Until a year ago, it was thought that solitons would eventually replace NRZ communications because of the demonstrated capability to do wavelength division multiplexing (WDM) with solitons. It was supposed that it would not be possible to do WDM with NRZ communications. However, it has recently been demonstrated that in fact WDM is possible with NRZ, and, while solitons are promising, NRZ systems remain a step ahead.[2] Thus, the future for solitons is unclear.

This situation is both an enigma and an enormous challenge to the theorist. Historically, NRZ communication systems came into vogue because in communication systems based on microwave RU-232 cable, signal distortion was dominated by dispersion and so it was desirable to minimize the bandwidth of the signal—something that NRZ signals accomplish quite well. For this reason, there has been a tendency to think of NRZ propagation as linear propagation, but that is simply not true! From a nonlinear standpoint, the behavior of soliton systems is not too hard too analyze because there is a well-defined sense in which a soliton is a pure mode of the nonlinear system.[1] By contrast, there is no sense in which NRZ pulses are modes, and, as a consequence, these systems are very difficult to study, and the theoretical work to date has had little predictive capability. Because neighboring NRZ bits interact, one must keep long strings of bits in the simulations which seriously slows down numerical calculations. The enigma and the challenge is to understand why these systems work as well as they do and to predict their ultimate limits.

It is already apparent that the large and rapidly varying birefringence that occurs in communication fibers plays a critical role in the distortion of NRZ pulses and in the ultimate bit error rates that can be achieved. Thus, understanding the impact of these variations is a crucial first step toward achieving an understanding of NRZ systems—not to mention that they play a vital role in soliton systems as well!

It is important to understand precisely what is meant when we describe the birefringence as large. Single mode optical fibers have one propagating mode that is referred to as the HE_{11} mode, but this mode is doubly degenerate. Doping and core anisotropies break the degeneracy, leading to birefringence, but typical values of $\Delta n/n$ are 10^{-7}–10^{-6}. While one might be tempted to think that this value is small, it implies a beat length that is on the order of 10 m, while nonlinear and dispersive effects occur on a length scale of 100–1000 km. Thus, it is actually very large! At the same time, one can infer from measurements to be described shortly that the fiber correlation length is on the order of 30–100 m, so that the birefringence is also rapidly varying. Thus, it makes sense to use multiple length scale techniques in which we first determine the evolution on the rapidly varying length scale of the randomly varying birefringence and then use the results to determine the evolution on the much longer dispersive and nonlinear length scales. Not only is this approach sensible from a conceptual standpoint, as it allows us to distinguish the phenomena occurring on the different length scales, but it will also allow us to create simulation codes that are significantly more efficient and accurate than those that are presently in use.

In this article, we will be concentrating on the rapidly varying length scale, and we will discuss its impact on the nonlinear evolution briefly at the end. We have actually only just begun to attack the full evolution, taking advantage of what we have learned on the rapidly varying length scale. The behavior on the rapidly varying length scale is linear but random, with the randomness being the major complication. At the end of the article, we will mention briefly some of the consequences of our calculations for the nonlinear evolution.

2. DIFFERENTIAL TIME DELAY

Experimentally, one finds that the randomly varying birefringence leads to a frequency-dependent differential time delay that in turn leads to pulse spreading.[3] One of the ways in which this delay manifests itself is that if the light from a multi-mode laser is injected into an optical fiber, it maps into a circle on the Poincaré sphere after propagating some length into the fiber. That implies that there are two orthogonal states, referred to as principal states, that to first order would not be spread on the Poincaré sphere by propagation through the fiber. The delay between these two states is the differential time delay because any other state is a combination of these two states and will arrive at some intermediate time. We begin by demonstrating the existence of the principal states and calculating the differential time delay. We then determine the expected distribution of the differential time delay as a function of distance along the fiber.

Taking a fixed set of axes, labeled 1 and 2, we may write the complex amplitudes of the two polarizations as a column vector $\mathbf{E} = (E_1, E_2)^t$, where E_1 and E_2 are functions of distance along the fiber z and frequency ω. The evolution of this column vector is governed by the linear equation

$$\frac{\partial \mathbf{E}(\omega, z)}{\partial z} = i\mathsf{K}(\omega, z)\mathbf{E}(\omega, z), \tag{1}$$

where

$$\mathsf{K} = k_0\mathsf{I} + \kappa_1\sigma_1 + \kappa_2\sigma_2 + \kappa_3\sigma_3, \tag{2}$$

and the σ_j are the usual Pauli matrices. We first note that if there is no polarization-dependent loss, then all the κ_j must be real. While, in fact, there is some polarization-dependent loss in the real systems, this loss occurs at the amplifiers, which are located 30–100 km apart, and its effect is small, although not unimportant. We will not consider it in this article. We include polarization-independent loss in the system by allowing k_0 to be complex, but it enters into the problem in a fairly trivial way. Making the transformation

$$\mathbf{A} = \mathbf{E} \exp\left[-i \int_0^z k_0(z')\, dz'\right], \tag{3}$$

we find that k_0 disappears from the evolution equation. Noting that optical fibers are linearly birefringent so that $\kappa_2 = 0$, we find that the evolution equation for A is

$$\frac{\partial \mathbf{A}(\omega, z)}{\partial z} = i\Theta(\omega, z)\mathbf{A}(\omega, z), \tag{4}$$

where

$$\Theta = \kappa_1\sigma_1 + \kappa_3\sigma_3 \equiv b\sin\theta\,\sigma_1 + b\cos\theta\,\sigma_3, \tag{5}$$

and b corresponds to the normalized birefringence strength while θ corresponds to the orientation of the birefringent axes. Since Θ is a traceless, Hermitian matrix at every ω, it follows that it generates a unitary transformation at every ω. Assuming now that this transformation matrix is sufficiently smooth as a function of ω, there must be at any z some traceless, Hermitian matrix F that satisfies

$$\frac{\partial \mathbf{A}}{\partial \omega} = i\mathsf{F}(\omega, z)\mathbf{A}(\omega, z). \tag{6}$$

Since this matrix F is traceless and Hermitian, its eigenvalues are real and have the same absolute values with opposite signs while its eigenvectors are orthogonal. Writing the eigenvectors as $\pm\tau_D/2$, it is not difficult to see that the eigenvalues correspond to $\pm$one-half the differential time delay while the eigenvectors correspond to the principal states. Solving Eq. (6), and writing the eigenvectors as S_p and $S_{p'}$, we find that

$$S_p(\omega, z) = S_p(0, z)\exp(i\tau_D\omega/2), \qquad S_{p'}(\omega, z) = S_{p'}(\omega, 0)\exp(-i\tau_D\omega/2). \tag{7}$$

When we use the Fourier transform to return to the time domain, it follows that an initial pulse that consists strictly of the initial state that transforms *via* Eq. (4) into S_p will have a time delay of $\tau_D/2$, and, similarly, an initial pulse that transforms into $S_{p'}$ will have a time delay $-\tau_D/2$. This result was obtained earlier by Poole and Wagner,[4] but their derivation was considerably more elaborate because they did not make use of the known properties of Hermitian matrices.

The next step is to determine the probability distribution of the differential time delay τ_D. Poole[5] has described an approach that applies in the limit in which there is a large and nearly fixed birefringence and in which there is a weak mode coupling. In this model $\cos\theta \simeq 1$ and $\sin\theta \simeq \theta$ in Eq. (4) so that Eq. (4) becomes

$$\frac{\partial A}{\partial z} = i\theta\sigma_1 + b\sigma_3, \tag{8}$$

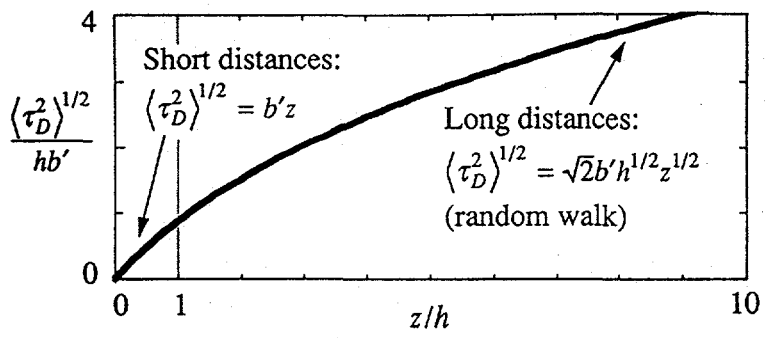

FIGURE 2. Variance of the differential time delay as a function of position along the fiber.

This limit is not really valid for communication fibers; however, we recently showed that a model that allows the birefringence orientation to vary randomly will yield the same results.[6] To obtain this result, it is useful to attempt to solve Eq. (5) through repeated diagonalization. Ignoring the variation of θ as a function of z, we could solve Eq. (4) by making the transformation $\mathbf{B}_1 = \mathsf{U}_1\mathbf{A}$ where

$$\mathsf{U}_1 = \cos(\theta/2)\,\mathsf{I} + i\sin(\theta/2)\,\sigma_3, \tag{9}$$

We then find that

$$\frac{\partial \mathbf{B}_1}{\partial z} = i\left(\mathsf{U}_1\Theta\mathsf{U}_1^{-1} - \mathsf{U}_1\frac{\partial \mathsf{U}_1^{-1}}{\partial z}\right)\mathbf{B}_1 \equiv i\Psi_1\mathbf{B}_1, \tag{10}$$

where U_1^{-1} is the inverse of U_1 and Ψ_1 can be written explictly as

$$\Psi_1 = \frac{1}{2}\frac{d\theta}{dz}\sigma_2 + b\sigma_3. \tag{11}$$

This equation is essentially the same as Eq. (8). The appearance of σ_2 rather than σ_1 makes no diffrence in the polarization mode dispersion. The only significant difference is that whereas Poole assumed that θ varies rapidly compared to the beat length, we must assume that $d\theta/dz$ varies rapidly compared to the beat length. In either case, one finds that the mean of the differential time delay is zero, and its variance is given by[5,6]

$$\langle \tau_D^2 \rangle^{1/2} = \sqrt{2}hb'\left[\exp(-z/h) - 1 + z/h\right]^{1/2}, \tag{12}$$

where $b' = db/d\omega$ is the derivative of the birefringence and h is a characteristic decorrelation length.

In the case of Poole's model, h corresponds to the length scale over which the polarizations mix. In the case of our model, it corresponds to the length over which the polarizations mix when measured in the frame that rotates with the local polarization axes. We note that in our model, $h = h_{\text{fiber}}$, where h_{fiber} is the correlation length for the optical fiber itself. Of course, in Poole's model, $h_{\text{fiber}} = \infty$ so that there is no relation

between h and h_{fiber}. Since one cannot directly measure the orientation of the polarization axes as a function of position along the fiber, it might appear at first that both models are equally plausible, but in fact, one can infer from the existence of solitons that the orientation must be randomly varying. Solitons tend to propagate naturally in a single polarization state,[7] and unless the orientation is randomly varying, solitons will be observed to split, and there is no evidence of that. Thus, we can use solitons to probe the structure of the fiber! We note that one can infer h from measurements of the differential time delay which is how it is measured in practice. Equation (12) is physically sensible. When z is small compared to the decorrelation length, then the two polarizations separate linearly in z. When z is large compared to the decorrelation length, then the two polarizations undergo a random walk and their separation is proportional to $z^{1/2}$.

To derive Eq. (12), we will present here an approach first described by Poole[5] and later modified by us so that it could be used to prove an ergodic theorem.[6] We have shown more recently that Eq. (12) can be derived more simply using the methods of stochastic differential equations; however, these results are still unpublished and cover a group of models that is less broad. Our starting point is to note that Eq. (10) that governs the evolution of $\mathbf{B}_1$ as a function of z is complemented by the equation

$$\frac{\partial \mathbf{B}_1}{\partial \omega} = i\mathsf{F}_1\mathbf{B}_1, \tag{13}$$

that governs the evolution of $\mathbf{B}_1$ as a function of ω, where F_1 is a traceless, Hermitian matrix. It then follows that $\tau_D^2 = -4\det \mathsf{F}_1 = 4\det(\partial \mathsf{T}_1/\partial\omega)$, where $\mathbf{B}_1(z,\omega) = \mathsf{T}_1(z,\omega)\mathbf{B}_{1,0}$. Defining now $\mathsf{S} = \exp\bigl[-i\phi(z)\sigma_3\bigr]\mathsf{T}_1$, where $\phi(z) = \int_0^z b(z')\,dz'$, we obtain

$$\frac{\partial \mathsf{S}}{\partial z} = \begin{pmatrix} 0 & \frac{1}{2}\theta_z \exp(-2i\phi) \\ -\frac{1}{2}\theta_z \exp(2i\phi) & 0 \end{pmatrix} \mathsf{S}, \tag{14}$$

where $\theta_z = d\theta/dz$. It now follows that

$$\tau_D^2 = 4\det(\mathsf{S}' + i\sigma_3\phi'\mathsf{S}), \tag{15}$$

where the primes indicate derivatives with respect to ω.

Writing the components of S explicitly so that

$$\mathsf{S} = \begin{pmatrix} s_1 & s_2 \\ -s_2^* & s_1^* \end{pmatrix}, \tag{16}$$

and taking the first derivative of τ_D^2, we obtain

$$\frac{\partial \tau_D^2}{\partial z} = 8b'\phi' + 8ib'(s_1 s_1'^* + s_2 s_2'^*), \tag{17}$$

where we assume that the elements of S are slowly varying so that we can neglect their variation with z. The key assumption is that the θ_z are small compared to b but vary rapidly so that their derivatives are large. Similarly, we find

$$\frac{\partial^2 \tau_D^2}{\partial z^2} = 4(b')^2 + 4\phi'\frac{db'}{dz} - 4ib'\theta_z\bigl(s_1 s_2' - s_1' s_2'\bigr)\exp(2i\phi) + \text{c.c.} \tag{18}$$

Although S is slowly varying, its z derivative varies rapidly, and we can use this fact to replace s_1 in Eq. (18) with the integral expression

$$s_1(z) \simeq s_1(\zeta) - \int_\zeta^z \frac{\theta_z(z')}{2} \exp\bigl[-2i\phi(z')\bigr]\, dz', \tag{19}$$

where $z-\zeta$ is a length that is long compared with the variation of θ_z and short compared with the variations of s_1 and s_2. The assumed existence of this intermediate length scale plays an important role in our argument. Similar results can be obtained for $s_2(z)$, $s_1'(z)$, and $s_2'(z)$. Defining

$$\begin{aligned} H(z) &= \mathrm{Re}\left[\int_\zeta^z \frac{\theta_z(z)\theta_z(z')}{4} \exp\bigl[2i\phi(z) - 2i\phi(z')\bigr]\, dz'\right] \\ &\simeq \frac{1}{2}\int_{-\infty}^{\infty} \frac{\theta(z)\theta(z')}{4} \exp\bigl[2i\phi(z) - 2i\phi(z')\bigr]\, dz', \end{aligned} \tag{20}$$

where we have used the assumed rapid variation of θ_z to extend the integral to $-\infty$, we may now rewrite Eq. (18) in the form

$$\frac{\partial^2 \tau_D^2}{\partial z^2} = 8(b')^2 + 8\phi'\frac{db'}{dz} - 32b'\phi' H(z) - 32ib' H(z)(s_1' s_1'^* + s_2 s_2'^*), \tag{21}$$

where we have dropped both small terms and rapidly varying terms that will not contribute on the length scale $z-\zeta$.

In order to obtain an ergodic theorem, our goal is to replace Poole's ensemble average over "a collection of statistically equivalent fibers" with an appropriate spatial average.[5,6] Since both b and θ change slowly by assumption, we may beplace $\phi(z)-\phi(z')$ with the local relationship $b(z-z')$. In general b and θ_z^2 are correlated; the latter is larger when the former is smaller. Consequently, b and H will be correlated. By contrast, we may assume that ϕ and $s_1 s_1'^* + s_2 s_2'^*$ are uncorrelated with b and H since these quantities are determined by integration from the origin and, over sufficiently long lengths, will be nearly independent of the local values of b and H. Physically, this length corresponds to the length over which the electric field samples the entire Poincaré sphere. Defining an ensemble average

$$\langle X(z)\rangle = \frac{1}{L}\int_{z-L}^{z} X(z')\, dz' \tag{22}$$

where L is this averaging length, we find, letting $\langle b'H\rangle = r\langle b'\rangle\langle H\rangle$, that

$$\langle \tau_D^2\rangle = \frac{\langle (b')^2\rangle}{2r^2\langle H\rangle^2}\bigl[\exp(-4r\langle H\rangle z) - 1 + 4r\langle H\rangle z\bigr]. \tag{23}$$

From the preceeding discussion, it should be apparent that this result is only meaningful in the limit $z \gg h$, where $h = 1/4r\langle H\rangle$.

Given $\langle \tau_D^2 \rangle$, the next task is to calculate the entire distribution function for τ_D^2. While this task has yet to be accomplished in general, it has been argued on physical grounds and verified in simulations that the actual distribution is given by

$$f(\tau_D^2) = \frac{2\tau_D^2}{\sqrt{\pi}\left(\langle \tau_D^2 \rangle / 3\right)^{3/2}} \exp\left(-3\tau_D^2 / \langle \tau_D^2 \rangle\right), \tag{24}$$

corresponding to a random walk on the Poincaré result. Determining the full evolution of the distribution function remains an important open problem.

3. DISCUSSION AND CONCLUSIONS

We showed in early work that in the limit of large but rapidly and randomly varying birefringence, the evolution of the field in the optical fiber is described by the Manakov equation,[7]

$$\begin{aligned} i\frac{\partial U}{\partial z} + \frac{1}{2}\frac{\partial^2 U}{\partial t^2} + \left(|U|^2 + |V|^2\right) U = 0, \\ i\frac{\partial U}{\partial z} + \frac{1}{2}\frac{\partial^2 U}{\partial t^2} + \left(|U|^2 + |V|^2\right) V = 0, \end{aligned} \tag{25}$$

where U and V correspond physically to the state that a linear, cw wave at the pulse's central frequency would occupy and its orthogonal complement. We now have models for the polarization mode dispersion that we know are physically correct. The next stage of this work is to combine the two effects to obtain a complete description of wave propagation through the fiber. This task is very important because large computational savings in modeling the fibers as well as an increase in understanding appear to be obtainable.

We expect to report progress along those lines in the very near future!

ACKNOWLEDGMENTS

This work was supported by the Department of Energy. Numerical work was carried out at SDSC and NERSC

REFERENCES

1. C. R. Menyuk, J. Opt. Soc. Am. B **10**, 1585 (1993).
2. See, N. S. Bergano, *et al.*, "40 Gbit/s WDM transmission of eight 5 Gb/s data channels over transoceanic distances using the conventional NRZ modulation format," presented at the OFC '95 meeting (February, 1995).
3. N. S. Bergano, C. D. Poole, and R. E. Wagner, J. Lightwave Technol. **5**, 1618 (1987).
4. C. D. Poole and R. E. Wagner, Electron. Lett. **22**, 1029 (1986).
5. C. D. Poole, Opt. Lett. **13**, 687 (1988).
6. C. R. Menyuk and P. K. A. Wai, J. Opt. Soc. Am. B **11**, 1288 (1994).
7. P. K. A. Wai, C. R. Menyuk, and H. H. Chen, Opt. Lett. **16**, 1231 (1991).

CONDITIONS FOR SYNCHRONIZATION IN JOSEPHSON-JUNCTION ARRAYS

A.A.Chernikov & G. Schmidt

Stevens Institute of Technology, Hoboken , NJ 07030

ABSTRACT

An effective perturbation theoretical method has been developed to study the dynamics of Josephson junction series arrays. It is shown that the inclusion of junction capacitances, often ignored, has a significant impact on synchronization. Comparison of analytic with computational results over a wide range of parameters shows excellent agreement.

INTRODUCTION

Josephson junctions are known to produce very high frequency oscillations and can be used to generate submillimeter range radiation [1-3]. The difficulty is the low power output of individual junctions. This could be remedied by the use of many synchronized coupled junctions. Fig.1 shows a sketch of N junctions in series, fed by a constant dc current source and shunted by a load of impedance Z. The junctions have an internal resistance as well as a capacitance.

In normalized units this circuit is described by

$$\beta\ddot{\varphi}_k + \dot{\varphi}_k + \sin(\varphi_k) + I_L = I \qquad (1)$$

where φ_k represents the phase difference of the wave function across the k-th junction, β corresponds to the capacitance of the junction, I_L is the load current. Without the load, the system can be visualized as a point particle of mass β sliding down an incline of steepness I, sinusoidally modulated, with air resistance represented by $\dot{\varphi}_k$. To maintain the motion and oscillations it is necessary that $I > 1$.

The load current depends on the voltage across the array, proportional to $\sum\dot{\varphi}_j$. For instance for a load made up of an inductance, capacitance and resistance in series one writes in normalized units

$$L\dot{I}_L + RI_L + (1/C)\int I_L dt = (1/N)\sum\dot{\varphi}_j \qquad (2)$$

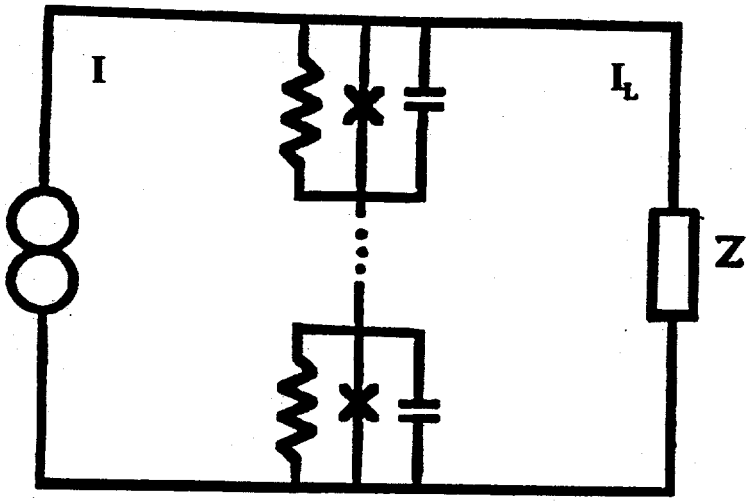

1. Sketch of the circuit investigated. Constant current I feeds the system, the junctions form an 1D array with resistive and capacitive characteristics, coupled to an impedance Z.

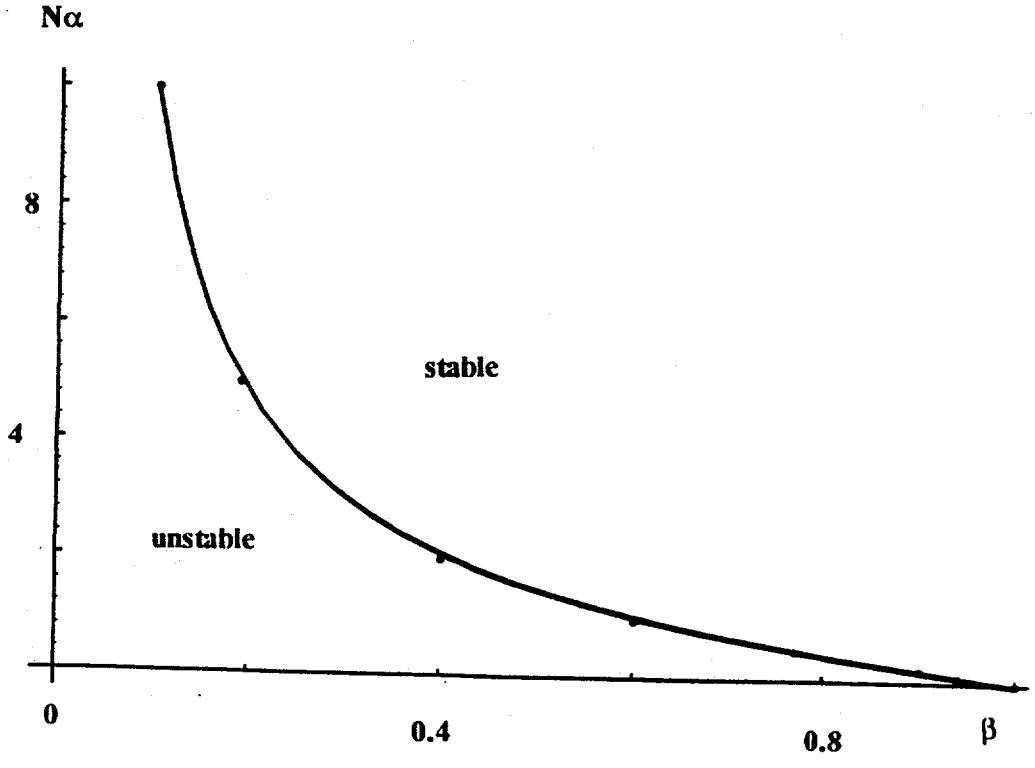

2. Computed dividing line between stable and unstable regions in β - αN parameter space of capacitively loaded arrays.

These equations are clearly nonlinear and no analytic solutions are available.

Recently several authors [4-9] investigated analytically a simplified version of these equations. The load capacitance has been ignored ($\beta = 0$) and the coupling to the load (I_L), has been assumed to be small, so perturbation theory could be used. Under these conditions it was shown that for a purely resistive load the equations are integrable [7] . The present authors have shown [9] that if a slight difference between the individual junction parameters is introduced, integrability fails and chaotic behavior follows. Quite recently Wiesenfeld and Swift [8] studied analytically the simplified equations of identical junctions with $\beta = 0$ in the weak coupling limit, and found that the synchronous solutions are stable if the load is predominantly inductive, and unstable if it is capacitive. The dividing line is at resonance when the Josephson junction frequency equals the resonant frequency of the load $(LC)^{-2}$.

Computed solutions of the equations show however that the junction capacitance has a significant effect on the stability of synchronized solutions, even for $\beta \ll 1$. Here a powerful perturbation theoretical method is developed where β as well as the coupling strength can be arbitrarily large, and excellent agreement is found with computer generated solutions.

CAPACITIVE LOAD; COMPUTATION

First we rewrite Eqs.(1) and (2), by dividing (1) by I, and rescaling time, $It \rightarrow t$, and $I\beta \rightarrow \beta$, to get

$$\beta\varphi_k + \varphi_k + b\sin(\varphi_k) + J = 1 \tag{3}$$

$$\mu_1 J + \mu_2 J + \int J dt = \alpha\sum\varphi_j \tag{4}$$

where $J = I_L/I$, $b = I^{-1}$, $\mu_1 = LCI^2$, $\mu_2 = RCI$, $\alpha = IC/N$. For a purely capacitive load $\mu_1 = \mu_2 = 0$, and these equations reduce to

$$\beta\,\varphi_k + \varphi_k + b\sin(\varphi_k) + \alpha\sum\varphi_j = 1 \tag{5}$$

In order to study the linear stability of the synchronous solution, one expand $\varphi_k = \varphi_0 + \delta\varphi_k$, where φ_0 satisfies the

$$\beta\varphi_0 + \varphi_0 + b\sin(\varphi_0) + N\alpha\varphi_0 = 1 \tag{6}$$

equation, while for $\delta\varphi_k$ one has

$$\beta\,\delta\varphi_k + \delta\varphi_k + b\cos(\varphi_0)\delta\varphi_k + \alpha\sum\varphi_j = 0 \tag{7}$$

Subtracting the k-th from l-th equation gives [5]

$$\beta\,\Delta_{l,k} + \Delta_{l,k} + b\cos(\varphi_0)\Delta_{l,k} = 0 \tag{8}$$

where $\Delta_{l,k} = \delta\varphi_l - \delta\varphi_k$. Linear stability implies that $\Delta_{l,k}$ asymptotically tends to zero. One solves Eq.(6) on the computer, for given parameters β, b and $N\alpha$, and the computed function φ_0 in Eq.(8) to determine, the long time behavior of $\Delta_{l,k}$. Since $I > 1$, the parameter b is always less than one.

b is always less than one.

Fig.2 shows the β - Nα curve constructed for b = 0.5, b = 0.25 and b = 0.1. Two important conclusions follow,

1., The three curves practically coincide, the differences are within the width of the line.

2., While for β = 0, the synchronous state is always linearly unstable, as expected [8] , for large coupling even the addition of small junction capacitance can stabilize the state. For example when Nα =10, $\beta > 0.1$ gives stability. When $\beta > 1$ stability persists for any value of the coupling.

The first condition suggest an analytic method. Since the solution is essentially independent of b, one can carry out an analytic calculation based on a small b expansion. Since b is the coefficient of the only nonlinear term, the expansion can be reduced to the solution of set of linear equations.

CAPACITIVE LOAD; ANALYSIS

To the lowest order in the expansion in b, Eq.(5) gives $\varphi_k = t + \theta_k$. First order terms are

$$\beta\ddot{\varphi}_k^{(1)} + \dot{\varphi}_k^{(1)} + \alpha\sum\ddot{\varphi}_j^{(1)} + b\sin(t + \theta_k) = 0 \qquad (9)$$

giving second order linear inhomogeneous equations, with oscillating solutions

$$\varphi_k^{(1)} = A_k \sin(t) + B_k \cos(t) \qquad (10)$$

where coefficients are determined from

$$\beta A_k + B_k + \alpha\sum A_j - b\cos\theta_k = 0, \qquad (11)$$

$$A_k - \beta B_k - \alpha\sum B_j + b\sin\theta_k = 0. \qquad (12)$$

Summation over all junctions gives

$$(\beta + N\alpha)\sum A_j + \sum B_j - b\sum\cos\theta_j = 0, \qquad (13)$$

$$-(\beta + N\alpha)\sum B_j + \sum A_j + b\sum\sin\theta_j = 0 \qquad (14)$$

with the solution

$$\sum A_j = b[1 + (\beta + N\alpha)^2]^{-1}[(\beta + N\alpha)\sum\cos\theta_j - \sum\sin\theta_j] \qquad (15)$$

$$\sum B_j = b[1 + (\beta + N\alpha)^2]^{-1}[(\beta + N\alpha)\sum\sin\theta_j + \sum\cos\theta_j] \qquad (16)$$

Substituting these expressions into Eqs.(11) and (12) gives

$$A_k = b(1 + \beta^2)^{-1}(-\sin\theta_k + \beta\cos\theta_k) + b\alpha(1 + \beta^2)^{-1}[1 + (\beta + \alpha N)^2]^{-1}$$
$$[(1 - \beta^2 - \beta\alpha N)\sum\cos\theta_j + (2\beta + \alpha N)\sum\sin\theta_j] \qquad (17)$$

$$B_k = b(1+\beta^2)^{-1}(\cos\theta_k + \beta\sin\theta_k) + b\alpha(1+\beta^2)^{-1}[1+(\beta + \alpha N)^2]^{-1}$$
$$[(1-\beta^2-\beta\alpha N)\sum\sin\theta_j - (2\beta+\alpha N)\sum\cos\theta_j] \quad (18)$$

The second order expansion of Eq.(5) gives

$$\beta\ddot{\varphi}_k^{(2)} + \dot{\varphi}_k^{(2)} + \alpha\sum\ddot{\varphi}_j^{(2)} + b\cos(t+\theta_k)\varphi_k^{(1)} = 0 \quad (19)$$

where $\varphi_k^{(1)}$ is given by Eqs.(10), (17) and (18). The driving term in Eq. (19) contains second harmonics as well as time independent terms. Synchronization as well as desynchronization is due to long time behavior, compared to the oscillation time scale. It is useful therefore to consider the time averaged term

$$\langle\, b\cos(t+\theta_k)\varphi_k^{(1)}\rangle = (b/2)(B_k\cos\theta_k - A_k\sin\theta_k) = (b^2/2)(1+\beta^2)^{-1} +$$
$$\alpha(b^2/2)(1+\beta^2)^{-1}[1+(\beta+\alpha N)^2]^{-1}[(1-\beta^2-\beta\alpha N)\sum\sin(\theta_j-\theta_k) - (2\beta+\alpha N)\sum\cos(\theta_j-\theta_k)] \quad (20)$$

So from Eqs. (19) and (20)

$$\varphi_k^{(2)} \sim -\langle\, b\cos(t+\theta_k)\varphi_k^{(1)}\rangle t + \text{second harmonic terms} \quad (21)$$

One may think of the φ_k-s as points moving on the unit circle. To lowest order they move with unit phase velocity separated by angles $\theta_j - \theta_k$. The first order solutions of Eq.(10) add oscillatory motion, while to second order, second harmonics of the oscillatory motion appear as well as a change in the time average velocity. The first term in Eq.(20) describes a slowing of all points to $1 - (b^2/2)(1+\beta^2)^{-1}$. The other two terms arise from the interaction of different points. Synchronization (or desynchronization) is described by the first of these terms. When $\beta = 0$ the angle differences $\theta_j - \theta_k$ grow toward a splay state. Past a threshold value of β the angle differences contract untill synchronization is achieved. This threshold is given by the equation

$$1 - \beta^2 - \beta\alpha N = 0 \quad (22)$$

This is an excellent fit to the curve in Fig.2.

Finally the last term in Eq.(20) describes the increase of phase velocities of points as they approach each other to the synchronous state, or the decrease of velocities as a splay state is approached.

ANALYSIS OF SYSTEM WITH RLC LOAD

A similar analysis can be carried out for the more general case described by Eqs. (3) and (4). This calculation is rather lengthy and here the detailes [10] are omitted, resulting in the synchronization condition

$$(1-\beta^2)(1-\mu_1) - \beta(2\mu_2 + \alpha N) < 0 \quad (23)$$

Various limiting cases follow. When the load is purely capacitive $\mu_1 = \mu_2 = 0$ and Eq.(22) is recovered.

When $\beta = 0$, the synchronization condition is

$$1 - \mu_1 = 1 - LCI^2 < 0 \qquad (24)$$

In our units the condition obtained by Wiesenfeld and Swift [8] is $LC(I^2 - 1) > 1$. For $b \ll 1$, $I \gg 1$ the two conditions agree.

When $\mu_1 = 1$, the system is in resonance and the synchronous state is always stable for $\beta > 0$.

Finally when driving current I is very large $\mu_1 \gg 1$, the condition becomes approximately

$$(1 - \beta^2) LI + \beta(2R + 1) > 0 \qquad (25)$$

independent of C.

It is clear that similar calculations can be carried out for an arbitrary load impedance Z (both for one-dimensional and two-dimensional arrays), leading to well defined conditions for synchronization or desynchronization. The growth rates of the instabilities leading to the final state are given by the coefficient of the $\sin(\theta_j - \theta_k)$ term.

ACKNOWLEDGEMENT

This work was sponsored by the U.S. Department of Energy, Contract No. DE-FGO2-87ER13740.

REFERENCES

1. K.Wan, A.K.Jain and J.E.Lukens, Appl. Phys. Lett., **51**, 1805 (1989).
2. S.Han, B.Bi, W.Zhang and J.E.Lukens, Appl. Phys. Lett., **64**, 1424 (1994).
3. M.J.Wengler, B.Guan and E.K.Track, IEEE Trans. on Microwave Theory and Techniques (submitted for publication).
4. K.Y.Tsang, R.E.Mirollo, S.H.Strogatz and K.Wiesenfeld, Physica D, **48**, 102 (1991).
5. P.Hadley, M.R.Beasley and K.Wiesenfeld, Appl. Phys. Lett., **32**, 1619 (1988).
6. S.Nichols and K. Wiesenfeld, Phys. Rev. E, **48**, 2569 (1993).
7. S.Watanabe and S.H.Strogatz, Physica D, **74**, 197 (1994).
8. K.Wiesenfeld and J.W.Swift, Phys. Rev. E, **51**, 1020 (1995).
9. A.Chernikov and G.Schmidt, Phys. Rev. E, **50** ,3436 (1994).
10. A.Chernikov and G.Schmidt, submitted for publication

MODELING ELECTRONEGATIVE PLASMA DISCHARGE

A. J. Lichtenberg and M. A. Lieberman

Department of Electrical Engineering and Computer Sciences
and the Electronics Research Laboratory
University of California, Berkeley, CA 94720

ABSTRACT

Macroscopic analytic models for a three-component electronegative gas discharge are developed. Assuming the negative ions to be in Boltzmann equilibrium, a positive ion ambipolar diffusion equation is derived. The discharge consists of an electronegative core and electropositive edges. The electron density in the core is nearly uniform, allowing a parabolic approximation to the plasma profile to be employed. The resulting equilibrium equations are solved analytically and matched to a constant mobility transport model of an electropositive edge plasma. The solutions are compared to a simulation of a parallel-plane r.f. driven oxygen plasma for $p = 50$ mTorr and $n_{eo} = 2.4 \times 10^{15}$ m^{-3}. The ratio α_0 of central negative ion density to electron density, and the electron temperature T_e, found in the simulation, are in reasonable agreement with the values calculated from the model. The model is extended to: (1) low pressures, where a variable mobility model is used in the electropositive edge region; and (2) high α_0 in which the edge region disappears. The inclusion of a second positive ion species, which can be very important in describing electronegative discharges used for materials processing, is a possible extension of the model.

I. INTRODUCTION

Considerable effort has gone into the development of equilibrium discharge models for electropositive plasmas. These include particle-in-cell (PIC) codes [1,2,3], fluid codes [4], and analytic approximations [5,6,7]. Plasma processing, however, usually involves electronegative gases and gas mixtures. The work presented here is based on and extends two models developed in our group to determine the behavior of oxygen discharges [8,9]. Oxygen is chosen both because of its usefulness in processing and because the reaction rates are relatively well known. In one study [8] a volume averaged two-dimensional model is developed, particularly for high plasma density (high power) low pressure discharges, which can be obtained, for example, in electron cyclotron resonance (ECR) and RF inductive sources. In a second study a theory is developed to treat an electronegative plasma with a planar spatial variation, at sufficiently high pressure that a constant mobility ion transport model is adequate, and when only a single positive ion species is important [9]. This situation applies to an oxygen discharge at low density and high pressure, in which dissociation of O_2 is not important. It was shown that the plasma is divided into a core electronegative region and an edge electropositive region, each with constant (but different) ambipolar diffusion coefficients [9]. Here, in addition to presenting some of the previous work, we develop a comprehensive, analytic, global model that is applicable over a wide range of pressures and powers. The model includes the relevant reaction rates appropriate to all of the significant ion and neutral species, as given in Ref. [8], which includes the presence of a second positive ion species. It also explicitly includes a core electronegative region with a surrounding electropositive region, but in a manner such that either region can essentially vanish in some parameter ranges. A Bohm condition for the particle flux at

the plasma-sheath edge, which is valid over the entire range of electronegativities, is used.

II. PHYSICS BASIS

A. *Global Equilibrium*

We previously considered the set of collisional reaction processes for an oxygen discharge as given in Table 1 [8].

Table 1. Model Reaction Set

Reaction			Rate Coefficients
$e + O_2$	$\longrightarrow$	$O_2^+ + 2e$	$k_1 = 9.0 \times 10^{-10} T_e^2 e^{-12.6/T}$ cm^3-s^{-1}
$e + O_2$	$\longrightarrow$	$O(^3P) + O(^1D) + e$	$k_2 = 5.0 \times 10^{-8} e^{-8.4/T}$ cm^3-s^{-1}
$e + O_2$	$\longrightarrow$	$O(^3P) + O^-$	$k_3 = 4.6 \times 10^{-11} e^{(2.91/T\ -12.6/T\ +6.92/T\ )}$cm^3-s^{-1}
$e + O(^3P)$	$\longrightarrow$	$O^+ + 2e$	$k_4 = 9.0 \times 10^{-9} T_e^{0.7} e^{-13.6/T}$ cm^3-s^{-1}
$O^- + O_2^+$	$\longrightarrow$	$O(^3P) + O_2$	$k_5 = 1.4 \times 10^{-7}$cm^3-s^{-1}
$O^- + O^+$	$\longrightarrow$	$O(^3P) + O(^3P)$	$k_6 = 2.7 \times 10^{-7}$cm^3-s^{-1}
$e + O^-$	$\longrightarrow$	$O(^3P) + 2e$	$k_7 = 1.73 \times 10^{-7} e^{(-5.67/T\ +7.3/T\ -3.48/T\ )}$cm^3-s^{-1}
$e + O_2$	$\longrightarrow$	$O(^3P) + O(^3P) + e$	$k_8 = 4.23 \times 10^{-9} e^{-5.56/T}$ cm^3-s^{-1}
$e + O(^3P)$	$\longrightarrow$	$O(^1D) + e$	$k_9 = 4.47 \times 10^{-9} e^{-2.286/T}$ cm^3-s^{-1}
$O(^1D) + O_2$	$\longrightarrow$	$O(^3P) + O_2$	$k_{10} = 4.1 \times 10^{-11}$cm^3-s^{-1}
$O(^1D) + O(^3P)$	$\longrightarrow$	$O(^3P) + O(^3P)$	$k_{11} = 8.1 \times 10^{-12}$cm^3-s^{-1}
$O(^1D)$	$\xrightarrow{\text{(wall)}}$	$O(^3P)$	$k_{12} = D_{\text{eff}}/\Lambda^2$ s^{-1}
$e + O(^1D)$	$\longrightarrow$	$O^+ + 2e$	$k_{13} = 9.0 \times 10^{-9} T_e^{0.7} e^{-11.6/T}$ cm^3-s^{-1}
O^+	$\xrightarrow{\text{(wall)}}$	$O(^3P)$	$k_{14} = 212.3\, T_e^{0.5}(2\pi r_p^2 h_L + 2\pi r_p 2\ell_p h_R)$ s^{-1}
O_2^+	$\xrightarrow{\text{(wall)}}$	O_2	$k_{15} = 149.9\, T_e^{0.5}(2\pi r_p^2 h_L + 2\pi r_p 2\ell_p h_R)$ s^{-1}

T_e [=] eV; p [=] mTorr.

Using these reactions for the creation and destruction of the various species, the simplest set of volume averaged global equilibrium equations assumes that the species densities are essentially constant in the bulk with density n, falling rapidly to a density n_s at the plasma-sheath edge. Keeping only the most important rate coefficients from Table 1, this yields the following equations: Neutral (O and O_2) particle balance:

$$2\,K_{diss} n_e n_{O2} = K_r n_O \quad ; \quad K_r = S/V, \tag{2.1}$$

$$G = K_{diss} n_e n_{O2} + K_r n_{O2} \tag{2.2}$$

Positive ion (O^+ and O_2^+) particle balance:

$$K_{iz1} n_e n_O = K_{rec1} n_- n_{1+} + n_{s1} u_{B1} (A_{loss}/V) \tag{2.3}$$

$$K_{iz2} n_e n_{O2} = K_{rec2} n_- n_{2+} + n_{s2} u_{B2} (A_{loss}/V) \tag{2.4}$$

Negative ion (O^-) particle balance:

$$K_{att} n_e n_{O2} = K_{rec1} n_- n_{1+} + K_{rec2} n_- n_{2+} \tag{2.5}$$

Power balance:

$$P_{abs} = (K_{iz1} n_e n_O \mathcal{E}_{c1} + K_{iz2} n_e n_{O2} \mathcal{E}_{c2}) V + (n_{s1} u_{B1} + n_{s2} u_{B2})(\mathcal{E}_{ew} + \mathcal{E}_{iw}) A_{loss} \tag{2.6}$$

Charge neutrality:

$$n_{1+} + n_{2+} = n_e + n_- \equiv n_e(1 + \alpha) \tag{2.7}$$

Here the densities n_{1+} and n_{2+} are the positive ion densities of O^+ and O_2^+, n_- is the density of O^-, S is the pumping speed, G is the O_2 source flow per unit volume, $\mathcal{E}_{c1}$ and $\mathcal{E}_{c2}$ are the collisional energy losses per ionization [8], $\mathcal{E}_{ew}$ and $\mathcal{E}_{iw}$ are the electron and ion energies lost per electron-ion pair lost to the wall, and V and A_{loss} are the plasma volume and plasma area for losses, respectively, and $u_{B1,2}$ are the Bohm velocities of O^+ and O_2^+. For ease of recognition we have renamed the reaction rates in Table 1: $K_{diss} \equiv k_8$, $K_{iz1} \equiv k_4$, $K_{iz2} \equiv k_1$, $K_{rec1} \equiv k_6$, $K_{rec2} \equiv k_5$, and $K_{att} \equiv k_3$. Reactions and rate coefficients omitted from the equations are of lesser importance, and excited states are ignored except in contributions to $\mathcal{E}_{c1}$ and $\mathcal{E}_{c2}$. For the neutral dynamics we assume a low fractional ionization and a low recombination coefficient at the walls for production of O_2 from O.

For a high power (high plasma density), low pressure (low neutral density) oxygen plasma discharge, as analyzed in Ref. [8], the neutral oxygen is nearly fully dissociated, the ratio $\alpha \equiv n_-/n_e \ll 1$, and the collisional regime is such that the variable mobility one dimensional solutions, as analyzed by Godyak and associates [5], are relative flat, except near the sheath edge. In this regime the set of equations (2.1)–(2.7) can be directly analyzed to obtain a reasonably accurate description of the plasma equilibrium.

B. *Spatially-Varying Three-Species Equilibrium*

In this model [9], we consider a subset (O_2^+, O^-, e) of charged particle species in a 1D (slab) geometry, and determine the spatially varying profiles of the species. We find that the discharge generally consists of an electronegative core, surrounded by electropositive edge regions in which $n_- \approx 0$. Depending on the parameters, the electropositive or electronegative regions can essentially vanish.

To determine the spatial variations, as in electropositive plasmas, for each charged species we write a flux equation

$$\Gamma_i = -D_i \nabla n_i \pm n_i \mu_i E_i, \tag{2.8}$$

where $D_i = kT_i/m_i\nu_i$, $\mu_i = |q_i|/m_i\nu_i$, with ν_i the total momentum transfer collision frequency and the $\pm$ corresponds to positive and negative carriers, respectively. In equilibrium the sum of the currents must balance,

$$\sum_{i=1}^{N} q_i \Gamma_i = 0. \tag{2.9}$$

If we make the additional assumption that both negative ion species are in Boltzmann equilibrium,

$$\frac{\nabla n_-}{n_-} = \gamma \frac{\nabla n_e}{n_e}, \tag{2.10}$$

where $\gamma = T_e/T_i$ (T_i is the temperature of both ionic species), then, using charge neutrality and the Einstein relations, together with (2.8)–(2.10), we obtain an approximate ambipolar diffusion coefficient for the positive ions

$$D_{a+} \approx D_+ \frac{1 + \gamma + 2\gamma\alpha}{1 + \gamma\alpha}. \tag{2.11}$$

The structure of D_{a+} is easily seen from (2.11). For $\alpha \gg 1$, γ cancels such that $D_{a+} \approx 2D_+$. When α decreases below 1, but $\gamma\alpha \gg 1$, $D_{a+} \approx D_+/\alpha$ such that D_{a+} increases inversely with decreasing α. For $\gamma\alpha < 1$, $D_{a+} \approx \gamma D_+$, which is the usual ambipolar diffusion without negative

ions. For plasmas in which $\alpha \gg 1$ at the plasma center the entire transition region takes place over a small range of $1/\gamma < \alpha < 1$, such that the simpler value of $D_{a+} = 2D_+$ holds over most of the electronegative plasma core, except near $n_- \approx 0$.

Consider now the positive ion diffusion equation, keeping only the dominant reaction rate constants, with only O_2^+ present. In plane-parallel geometry we have

$$-\frac{d}{dx}\left(D_{a+}(\alpha)\frac{dn_+}{dx}\right) = K_{iz}n_{O2}n_e - K_{rec}n_+n_-, \tag{2.12}$$

where n_{O2} is the neutral gas density. We eliminate n_e (through charge neutrality) and n_- (through α), to obtain

$$-\frac{d}{dx}\left(D_{a+}(n_+)\frac{dn_+}{dx}\right) = K_{iz}n_{O2}n_e(n_+) - K_{rec}n_+n_-(n_+) \tag{2.13}$$

where $D_{a+}(n_+)$ given by (2.11) is a complicated function of n_+ and three constants $\alpha_0 = n_{-0}/n_{e0}$ the ratio of n_- to n_e at the plasma center, n_{e0}, and T_e. To determine the three constants we use:

positive ion particle balance,

$$-D_{a+}\frac{dn_+}{dx}\bigg|_{x=\ell} = \int_0^\ell K_{iz}n_{O2}n_e dx - \int_0^\ell K_{rec}n_+n_-(n_+)dx; \tag{2.14}$$

negative ion particle balance,

$$\int_0^\ell K_{att}n_{O2}n_e dx - \int_0^\ell K_{rec}n_+n_-(n_+)dx = 0; \tag{2.15}$$

and energy balance,

$$P_{abs} = 2\mathcal{E}_c\int_0^\ell K_{iz}n_{O2}n_e dx + 2\mathcal{E}_w n_+(\ell_p)u_B \tag{2.16}$$

where $\mathcal{E}_c(T_e)$, the collisional energy lost per electron-positive ion pair created, is a known function of T_e, and $2\mathcal{E}_w n_+(\ell_p)u_B$ is the kinetic energy lost to the wall. Given the plasma length $2\ell_p$, and power P_{abs}, the three equations can be simultaneously solved for the three unknowns T_e, α_0, and n_{+0}. However, the plasma edge ℓ_p is not exactly known, but is dependent on the Bohm flux condition

$$-D_{a+}\frac{dn_+}{dx}\bigg|_{x=\ell} = n_+(\ell_p)u_B(T_e, T_i, \alpha), \tag{2.17}$$

which indicates where the sheath begins. Here $\alpha = \alpha(\ell_p) = n_-(\ell_p)/n_e(\ell_p)$. Since negative ions may be present when (2.17) is satisfied, the Bohm velocity may have the more general form [10]

$$u_B = \left[\frac{eT_e(1+\alpha)}{M_+(1+\gamma\alpha)}\right]^{1/2}, \tag{2.18}$$

which reduces to the usual expression $u_B = (eT_e/M_+)^{1/2}$ when $\alpha = 0$. For $\alpha > 1/\gamma$, the negative ions significantly reduce the Bohm velocity.

There are three different electronegative discharge equilibrium regimes depending on neutral pressure and applied power. (1) At low pressure and high power, α_0 is small. The negative ion density becomes quite small well within the plasma volume, such that the plasma can be treated as if it is essentially electropositive. (2) In the opposite limit of high pressure and low power, $\alpha_0 \gg 1$ and a significant density of negative ions may exist, which, from (2.18), gives a significantly depressed

Bohm velocity with essentially no electropositive edge regions. (3) An intermediate regime can exist where the central α may be quite large but a significant edge region has α near zero, allowing the usual Bohm velocity to be used at the plasma edge.

III. APPROXIMATE SOLUTIONS

A. *Three Component Model with Electronegative and Electropositive Regions*

Consider, as in previous work [9], that a central region of the discharge exists in which α is sufficiently large that $D_{a+} \approx 2D_+$, but that the effect of positive-negative ion recombination can be neglected in determining the spatial distribution. The diffusion equation (2.13) then takes the simple form

$$-2D_+ \frac{d^2 n_+}{dx^2} = K_{iz} n_{O2} n_{e0},$$

where (2.10) with $\gamma \gg 1$ allows us to set $n_e \approx n_{e0}$. In this approximation $n_+(x)$ has a simple parabolic solution of the form

$$\frac{n_+}{n_{e0}} = \frac{n_-}{n_{e0}} + 1 = \alpha_0 \left(1 - \frac{x^2}{\ell^2}\right) + 1, \tag{3.1}$$

where ℓ is the nominal position where $\alpha = 0$ (see Fig. 1). The $\alpha \gg 1$ solution is matched to an $\alpha = 0$ electropositive edge solution, which in turn determines the position of the plasma edge satisfying (2.17). The analysis is simplified by assuming that n_{e0} is known. The absorbed power P_{abs} is then obtained *a posteriori* from (2.16). If P_{abs} is specified rather than n_{e0}, then n_{e0} can be obtained iteratively, as is done for T_e, as described below.

In the development that follows we use the parabolic profile. However to allow the results to be used at small α_0, we use an average value of the diffusion coefficient obtained by substituting an average $\alpha = \bar{\alpha}$, where $\bar{\alpha} = \frac{2}{3}\alpha_0$ in the parabolic approximation.

Substituting this averaged $\bar{D}_{a+}$ in (2.14) and (2.15) and integrating, we obtain, respectively,

$$K_{iz} n_{O2} \ell = K_{rec} n_{e0} \left(\frac{8}{15}\alpha_0^2 + \frac{2}{3}\alpha_0\right) \ell + \frac{2\bar{D}_{a+}\alpha_0}{\ell}, \tag{3.2}$$

$$K_{att} n_{O2} \ell_p = K_{rec} n_{e0} \left(\frac{8}{15}\alpha_0^2 + \frac{2}{3}\alpha_0\right) \ell, \tag{3.3}$$

where in (3.2) the integration is only over the strongly electronegative plasma. At $x = \ell$ this electronegative solution is matched to an electropositive edge solution. The electropositive solution could be a sinusoidal profile, at higher pressures, a more nearly constant profile, at lower pressures, or a profile intermediate between the two. In previous work a parabolic profile was assumed in the electropositive region also, and the fluxes matched at the interface between the regions, to solve for the ratio ℓ/ℓ_p [9]. Here, in order to accommodate the flatter profile at lower pressures, we use a somewhat more general approach.

First, assuming ℓ/ℓ_p is known, we solve (3.3) to obtain

$$\alpha_0 = -\frac{5}{8} + \sqrt{\left(\frac{5}{8}\right)^2 + \frac{15}{8}\frac{K_{att}}{K_{rec}}\frac{n_{O2}}{n_{e0}}\frac{\ell_p}{\ell}}. \tag{3.4}$$

Since ℓ/ℓ_p is near unity for large α_0, the weak dependence on ℓ_p/ℓ is not significant; once a complete solution is found, the value of α_0 can be improved by iteration. For large α_0 (3.4) exhibits the important scaling $\alpha_0 \propto (n_{O2}/n_{e0})^{1/2}$. To obtain a relatively simple overall solution we also make

the assumption that the density in the electropositive solution is relatively constant, except very near the sheath, such that n_e can be set equal to n_{e0} in the integral term in (2.14). In this approximation particle conservation in the electropositive region yields

$$\frac{2\bar{D}_{a+}\alpha_0 n_{e0}}{\ell} + K_{iz} n_{O2} n_{e0}(\ell_p - \ell) = n_{e0} h_\ell u_B, \tag{3.5}$$

where $h_\ell \equiv n_s/n_{e0}$ can be obtained in various approximations. As in previous work [9], the temperature sensitive term K_{iz} can be eliminated by substituting K_{iz} from (3.2) into (3.5) to obtain

$$2\bar{D}_{a+}\alpha_0 \frac{\ell_p}{\ell^2} + K_{rec} n_{e0} \left(\frac{8}{15}\alpha_0^2 + \frac{2}{3}\alpha_0\right)(\ell_p - \ell) = h_\ell u_B. \tag{3.6}$$

which is valid provided $\ell/\ell_p < 1$. Equations (3.4), (3.6), and (3.2) can be solved simultaneously for α_0, ℓ/ℓ_p, and T_e, given n_{e0} as the independent parameter. Alternatively, a useful analytic method is to iteratively solve (3.4) and (3.6), which are not very sensitive to T_e, with an assumed T_e and then use (3.2) to iteratively improve the estimate of T_e. The procedure converges rapidly [9]. The power absorbed is then obtained from (2.16).

We give a comparison of the results of PIC simulation with the model, in Fig. 1, for a higher p case in which the constant mobility ion transport model for the electropositive edge is reasonable. The results indicate that the parabolic approximation is good in the electronegative region. Computing an effective electron temperature from $T_e = \frac{2}{3}\langle E \rangle$ we find $T_e = 2$eV in the PIC simulation and $T_e = 2.05$eV from the model, an excellent agreement. In Fig. 1 the central model density is normalized to that of the PIC simulation to compare the profiles. An $\alpha_0 = 11$, obtained from the model, is 30 percent larger than the $\alpha_0 = 8$ obtained from the simulation.

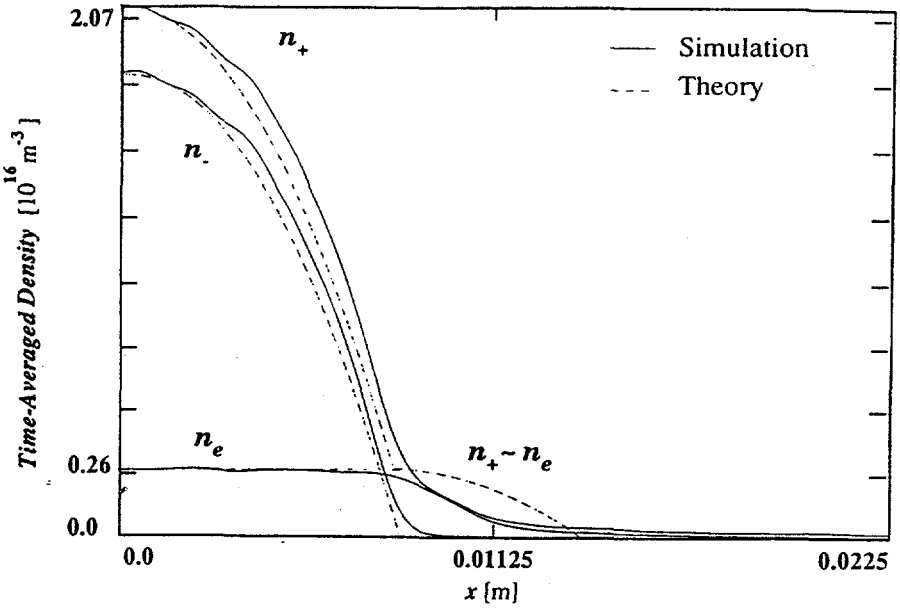

Figure 1. Comparison of analytic solution with simulation; n_{e0} and ℓ_p (at $u_i = u_B$) in the analytic solution are matched to the simulation; $p = 50$ mTorr and $n_{e0} = 2.4 \cdot 10^{15}$ m^{-3}; constant mobility model is used in the electropositive region.

B. *One Region Solution for Large Electronegativity*

For sufficiently large α_0 the electropositive edge region disappears. Assuming that the parabolic

solution is still a reasonable approximation for the negative ions

$$n_- = n_{e0}\alpha_0\left(1-\frac{x^2}{\ell^2}\right), \quad x < \ell_p,$$

but with $\ell > \ell_p$, then the particle balance equation for positive ions is

$$\begin{aligned} K_{iz}n_{O2}n_{e0}\ell_p =& K_{rec}n_{e0}^2\left\{\alpha_0^2\ell_p\left(1-\frac{2}{3}\frac{\ell_p^2}{\ell^2}+\frac{1}{5}\frac{\ell_p^4}{\ell^4}\right)+\alpha_0\ell_p\left(1-\frac{1}{3}\frac{\ell_p^2}{\ell^2}\right)\right\} \\ &+ n_{e0}\left[\alpha_0\left(1-\frac{\ell_p^2}{\ell^2}\right)+1\right]u_B \end{aligned} \tag{3.7}$$

where u_B is given by (2.18) with

$$\alpha = \alpha_0\left(1-\frac{\ell_p^2}{\ell^2}\right). \tag{3.8}$$

The negative ion particle balance is

$$K_{att}n_{O2}n_{e0}\ell_p = K_{rec}n_{e0}^2\left\{\quad\cdot\quad\right\}, \tag{3.9}$$

with the $\{\cdot\}$ repeated from (3.7). The third equation to complete the set is matching the positive ion edge flux

$$2\bar{D}_{a+}\alpha_0 n_{e0}\frac{\ell_p}{\ell^2} = n_{e0}\left[\alpha_0\left(1-\frac{\ell_p^2}{\ell^2}\right)+1\right]u_B. \tag{3.10}$$

For $\alpha_0 \gg 1$, keeping only the terms quadratic in α_0 in (3.9), we obtain

$$\alpha_0 = \left(\frac{K_{att}n_{O2}}{K_{rec}n_{e0}}\right)^{1/2}\left(1-\frac{2}{3}\frac{\ell_p^2}{\ell^2}+\frac{1}{5}\frac{\ell_p^4}{\ell^4}\right)^{-1/2}. \tag{3.11}$$

From (3.10)

$$\frac{\ell^2}{\ell_p^2} = \frac{\alpha_0\left(\dfrac{2\bar{D}_{a+}}{u_B\ell_p}+1\right)}{\alpha_0+1}. \tag{3.12}$$

Using these equations we have been able to explore the transition from a two region regime to a one region regime as the electronegativity α_0 increases. This is shown in Fig. 2, where the solid line for $\ell/\ell_p < 1$ (two region regime) is to be compared with the diamonds for $\ell/\ell_p > 1$ (entire plasma electronegative). The jump in ℓ/ℓ_p is caused by a jump in Bohm velocity in the somewhat idealized treatment. However, there is a hidden restriction, that has not been taken account in the two region model, which is that the ion flow cannot exceed the ion sound velocity. When this restriction is imposed (slightly modifying the theoretical treatment), the solid dots are obtained, giving an essentially continuous solution.

C. *Extensions to Multi-Component Plasmas and to Better Approximations*

The analysis presented above can be extended to additional plasma components. For oxygen, as described in Sec. II, O and O^+ must also be included if the analysis is to be applicable to a wide range of pressure and power. A set of equations have been obtained for two positive ion species

(four total species) using the same approximations as in sections A and B. We are in the process of determining the solutions to these equations over various ranges of pressure and power. We are also exploring better approximations to treat both the electronegative region at large α, and the electropositive edges at intermediate-to-low α.

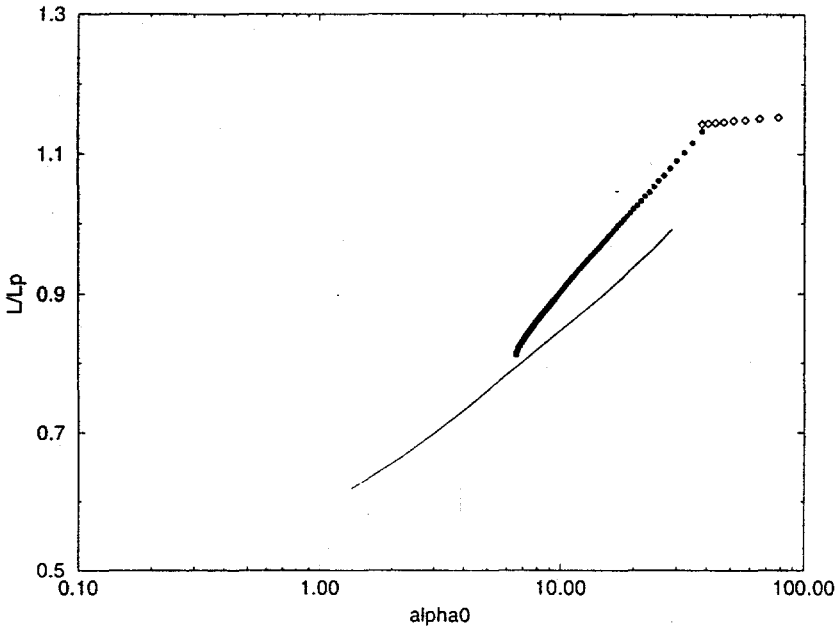

Figure 2. Analytic results of ℓ/ℓ_p is α_0 as n_{e0} is varied; $p = 50$ mTorr; variable mobility model is used in the electropositive region.

REFERENCES

1. D. Vender and R. Boswell, *IEEE Trans. Plasma Sci.*, **18,** 725 (1990).
2. M. Surendra and D. B. Graves, *IEEE Trans. Plasma Sci.*, **19,** 144 (1991).
3. B. Wood, "Sheath Heating in Low Pressure Capacitive R.F. Discharges," Thesis, University of California, Berkeley (1991).
4. D. B. Graves and K. F. Jensen, *IEEE Trans. Plasma Sci.*, **14,** 18 (1986).
5. V. A. Godyak, *Soviet Radio Frequency Discharge Research*, Delphic Assoc. Inc., Falls Church, VA (1986).
6. G. R. Misium, A. J. Lichtenberg, and M. A. Lieberman, *J. Vac. Sci. Technol.*, **A7,** 1007 (1989).
7. B. Wood, M. A. Lieberman, and A. J. Lichtenberg, *IEEE Trans. Plasma Sci.*, **23,** 89 (1995).
8. C. Lee, D. B. Graves, M. A. Lieberman, and D. W. Hess, *J. Electrochem. Soc.*, **141,** 1546 (1994).
9. A. J. Lichtenberg, V. Vahedi, M. A. Lieberman, and T. Rognlien, *J. Appl. Phys.*, **75,** 2339 (1994).
10. R. L. F. Boyd and J. B. Thompson, *Proc. Royal Soc.*, **A252,** 102 (1959).

PLASMA CHARACTERIZATION STUDIES FOR MATERIALS PROCESSING

E. Pfender and J. Heberlein

University of Minnesota
Minneapolis, MN 55455

ABSTRACT

New applications for plasma processing of materials require a more detailed understanding of the fundamental processes occurring in the processing reactors. We have developed reactors offering specific advantages for materials processing, and we are using modeling and diagnostic techniques for the characterization of these reactors. The emphasis is in part set by the interest shown by industry pursuing specific plasma processing applications. In this paper we report on the modeling of radio frequency plasma reactors for use in materials synthesis, and on the characterization of the high rate diamond deposition process using liquid precursors. In the radio frequency plasma torch model, the influence of specific design changes such as the location of the excitation coil on the enthalpy flow distribution is investigated for oxygen and air as plasma gases. The diamond deposition with liquid precursors has identified the efficient mass transport in form of liquid droplets into the boundary layer as responsible for high growth, and the chemical properties of the liquid for the film morphology.

INTRODUCTION

Plasma processing of materials continues to be a growing area, with specific applications ranging from plasma spray coatings to synthesis of ultrafine particles, from high rate deposition of diamond films using a thermal plasma CVD process to destruction of hazardous wastes. The increasing importance of this technical area is demonstrated by the fact that industry is increasingly making use of basic results obtained under this program, and providing additional funding thus leveraging the DOE funded effort.

In previous characterization efforts we had shown that many diagnostic techniques relying on line-of-sight or on time averaged measurements have limited value for characterizing plasma reactors with highly turbulent and reacting flows [1,2]. To improve our capability for describing plasma reactors used for materials processing, we have chosen (a) new diagnostic approaches relying on locally and/or temporally resolved measurement techniques, and (b) new modeling approaches. Two new diagnostic methods are being employed, the first being a high speed laser strobe video system, the second being based on laser scattering techniques developed at the Idaho

National Engineering Laboratory [3]. The new models have addressed issues of practical importance to materials processing reactors, such as radio frequency induction (RFI) plasma reactors with unusual geometries and different processing gases, and of d.c. arc jets either highly turbulent as used for atmospheric pressure plasma spraying, or possessing supersonic velocities with gases used for the deposition of diamond films. In this paper we will focus on two major efforts: (a) the description of the modeling approach and results of the RFI plasma reactor model, and (b) the experimental characterization of the novel method for diamond film deposition at ultra-high rates using liquid precursors. It should be noted that three additional efforts have been initiated for characterizing processing plasmas which cannot be discussed here due to space limitations: (1) the set-up and initial results of the laser scattering system for characterization of non-uniform, flowing plasmas, (2) the modeling of the diamond deposition process with liquid precursors, and (3) the application of the thermal plasma CVD process to the deposition of dense yttria stabilized zirconia films as they are used as electrolyte in solid oxide fuel cells.

MODELING OF HIGH-FREQUENCY (RF) PLASMA REACTORS

The application of RF plasma reactors for the synthesis of fine particles, for thermal plasma chemical vapor deposition (TPCVD), and for toxic waste destruction has been attracting increasing interest in recent years. RF plasmas are particularly suited for the synthesis of fine particles and for TPCVD if purity of the product is a primary concern, because electrode contamination is avoided. Toxic waste destruction with RF plasmas, on the other hand, offers the advantage of compatibility even with corrosive substances, since there are no electrodes in contact with the plasma.

For a better understanding of the characteristic features and for potential scale-up of such reactors, extensive modeling work has been conducted over the past two years. This work has laid the basis for additional funding from industry leveraging the DOE support.

Although modeling of RF plasma reactors has been previously reported, mainly with argon as working gas[1,2], in this modeling work, two different configurations and working gases have been considered, guided by potential applications. In case 1 our efforts focused on the conditions within the reactor itself with oxygen as working gas. In case 2, the plasma tail flame emanating from the reactor was of particular interest with air as the working gas. Because of space limitations, only the most important findings will be discussed in this paper.

Since the basic equations are the same for both cases, these equations will be briefly discussed in this paper.

Continuity: $$\frac{\partial(\rho u)}{\partial z}+\frac{1}{r}\frac{\partial(\rho r v)}{\partial r}=0 \qquad (1)$$

where ρ, u, v are the density, axial velocity and radial velocity respectively.

z-momentum:

$$\rho u\frac{\partial u}{\partial z}+\rho v\frac{\partial v}{\partial r}=-\frac{\partial P}{\partial r}+2\frac{\partial}{\partial z}\left(\mu_e\frac{\partial u}{\partial z}\right)+\frac{1}{r}\frac{\partial}{\partial r}\left[\mu_e r\left(\frac{\partial u}{\partial r}+\frac{\partial v}{\partial z}\right)\right]+\rho g+F_z \qquad (2)$$

where P is the pressure, F_z is the body force in the z-direction, and $\mu_e = \mu_l + \mu_t$ (μ_l : laminar viscosity, μ_t: turbulent viscosity)

r-momentum:

$$\rho u\frac{\partial u}{\partial z}+\rho v\frac{\partial v}{\partial r}=-\frac{\partial P}{\partial r}+\frac{2}{r}\frac{\partial}{\partial r}\left(\mu_e r\frac{\partial v}{\partial r}\right)+\frac{\partial}{\partial z}\left[\mu_e\left(\frac{\partial v}{\partial z}+\frac{\partial u}{\partial r}\right)\right]-\frac{2\mu_e v}{r^2}+\frac{\rho w^2}{r}+F_r \qquad (3)$$

where w is the tangential velocity and F_r is the body force in the r-direction.

θ-momentum:

$$\rho u\frac{\partial(rw)}{\partial z}+\rho v\frac{\partial(rw)}{\partial r}=\frac{\partial}{\partial z}\left(\mu_e\frac{\partial(rw)}{\partial z}\right)+\frac{1}{r}\frac{\partial}{\partial r}\left(\mu_e r\frac{\partial(rw)}{\partial r}\right)-\frac{2}{r}\frac{\partial}{\partial r}(\mu_e rw) \tag{4}$$

where w is the tangential velocity.

Energy:

$$\rho u\frac{\partial h}{\partial z}+\rho v\frac{\partial h}{\partial r}=\frac{\partial}{\partial z}\left(\frac{\lambda}{C_p}\frac{\partial h}{\partial z}\right)+\frac{1}{r}\frac{\partial}{\partial r}\left[\frac{\lambda}{C_p}r\frac{\partial h}{\partial r}\right]+\overline{q}_J-q_R \tag{5}$$

where h is the gas enthalpy, C_p is the specific heat, q_J is the Joule heating term, and q_R are the radiative heat losses.

Vector potential equations (see Ref. 3):

$$\frac{\partial^2 A_R}{\partial z^2}+\frac{1}{r}\frac{\partial}{\partial r}\left(r\frac{\partial A_R}{\partial r}\right)-\frac{A_R}{r^2}+\mu_0\sigma\omega A_I=0 \quad \frac{\partial^2 A_I}{\partial z^2}+\frac{1}{r}\frac{\partial}{\partial r}\left(r\frac{\partial A_I}{\partial r}\right)-\frac{A_I}{r^2}+\mu_0\sigma\omega A_R=0 \tag{6}$$

where A_R and A_I are the real and the imaginary parts of the vector potential A_θ. The electric and the magnetic fields are related to the vector potential by the following:

$$E_\theta=-i\omega A_\theta \qquad \mu_0 H_z=\frac{1}{r}\frac{\partial}{\partial r}(rA_\theta) \qquad \mu_0 H_r=-\frac{\partial}{\partial z}(A_\theta) \tag{7}$$

The radial and axial body forces acting on the plasma F_r, F_z, and the volumetric heat generation due to the Joule heating q_J are:

$$F_r=\frac{1}{2}\mu_0\sigma\mathrm{Real}\left[E_\theta H_z^*\right] \qquad F_z=-\frac{1}{2}\mu_0\sigma\mathrm{Real}\left[E_\theta H_r^*\right] \qquad q_J=\frac{1}{2}\sigma\left[E_\theta E_\theta^*\right] \tag{9}$$

where * denotes complex conjugate quantities.

Turbulent kinetic energy, k:

$$\rho u\frac{\partial k}{\partial z}+\rho v\frac{\partial k}{\partial r}=\frac{\partial}{\partial z}\left(\left(\mu_l+\frac{\mu_t}{\sigma_k}\right)\frac{\partial k}{\partial z}\right)+\frac{1}{r}\frac{\partial}{\partial r}\left[r\left(\mu_l+\frac{\mu_t}{\sigma_k}\right)\frac{\partial k}{\partial r}\right]+G-\rho\varepsilon \tag{10}$$

where

$$G=\mu_t\left\{2\left[\left(\frac{\partial u}{\partial z}\right)^2+\left(\frac{\partial v}{\partial r}\right)^2+\left(\frac{v}{r}\right)^2\right]+\left[r\frac{\partial}{\partial r}\left(\frac{w}{r}\right)\right]^2+\left(\frac{\partial u}{\partial r}+\frac{\partial v}{\partial z}\right)^2+\left(\frac{\partial w}{\partial z}\right)^2\right\} \tag{11}$$

Dissipation rate of turbulent kinetic energy, ε:

$$\rho u\frac{\partial \varepsilon}{\partial z}+\rho v\frac{\partial \varepsilon}{\partial r}=\frac{\partial}{\partial z}\left(\left(\mu_l+\frac{\mu_t}{\sigma_\varepsilon}\right)\frac{\partial \varepsilon}{\partial z}\right)+\frac{1}{r}\frac{\partial}{\partial r}\left[r\left(\mu_l+\frac{\mu_t}{\sigma_\varepsilon}\right)\frac{\partial \varepsilon}{\partial r}\right]+\frac{\varepsilon}{k}\left(C_{\varepsilon 1}f_{\varepsilon 1}G-C_{\varepsilon 2}f_{\varepsilon 2}\rho\varepsilon\right) \tag{12}$$

where C_μ, $C_{\varepsilon 1}$, $C_{\varepsilon 2}$, σ_h, σ_k and σ_ε are empirical constants of the k-ε turbulence model [4,5]:

C_μ	$C_{\varepsilon 1}$	$C_{\varepsilon 2}$	σ_h	σ_k	σ_ε
0.09	1.92	1.44	0.9	1.0	1.3

and the corrections $f_{\varepsilon 1}$ and $f_{\varepsilon 2}$ in the ε equations are given by

$$f_{\varepsilon 1}=1+\left(\frac{0.05}{f_\mu}\right) \qquad f_{\varepsilon 2}=1-\exp\left(-R_t^2\right)$$

The Lam-Bremhorst form of the Low-Reynolds-Number k-ε model is given by:

$$\mu_t = C_\mu f_\mu \frac{\rho k^2}{\varepsilon} \quad \text{where} \quad f_\mu = \left[1 - \exp\left(-0.0165 R_y\right)^2\right] \cdot \left(1 + \frac{20.5}{R_t}\right)$$

$$\text{with } R_y = \frac{\rho \sqrt{k}\, y}{\mu_t} \quad \text{and } R_t = \frac{\rho k^2}{\mu_t \varepsilon}$$

Results - Case 1:

A computer program has been developed to model the temperature and flow fields inside an RF plasma reactor for oxygen plasmas. This program is based on the SIMPLER algorithm [6]. The program solves the equations of conservation of mass (continuity), conservation of momentum and conservation of energy simultaneously. The source terms of the momentum and energy equations are supplied by the solutions from the vector potential equations (partial differential equations) of the electromagnetic field. In addition, a low Reynolds number, k-ε model is employed to model the turbulence in the plasma. The diffusive term of the momentum equations (effective viscosity) are supplied by solving the turbulent kinetic energy equations (k) and the turbulent kinetic energy dissipation rate equations (ε). The strong intercoupling between the partial differential equations makes modeling of RF plasmas a complex task.

A schematic of the RF plasma torch with the computational domain and geometry is shown in Figure 1. Based on the assumption of rotational symmetry, steady flow, local thermodynamic equilibrium (LTE), and optically thin conditions, solutions of the conservation equations have been obtained in terms of temperature and flow fields. Plasma properties and plasma compositions are calculated using the PLASMA code developed at the High Temperature Laboratory at the University of Minnesota.

As an example, Fig. 2 shows temperature and flow profiles at power levels from 10 to 30

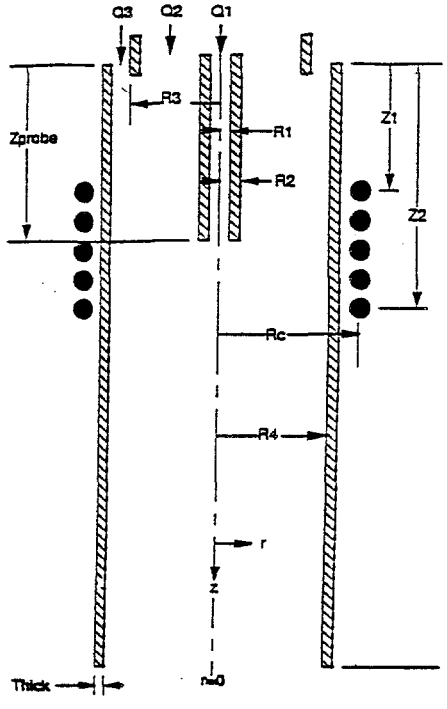

Fig. 1: Schematic of the RF plasma torch (Case 1)

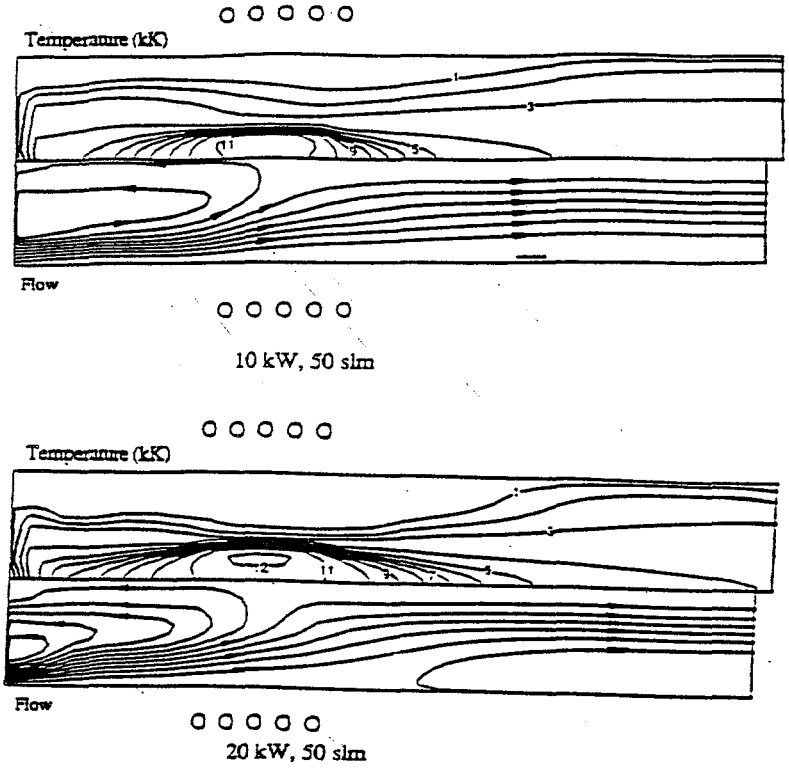

Fig. 2: Temperature and flow fields of oxygen plasmas at two power levels

kW and a gas flow rate of 50 slm. The maximum temperature in the plasma (approximately 12,000 K) remains almost the same as the power dissipation in the plasma increases, but the volume of hot plasma expands downstream. This behavior is typical for thermal RF plasmas.

Results - Case 2:

The same approach and essentially the same assumptions have been used to model temperature and flow fields for the RF plasma reactor configuration shown in Fig. 3, but in this case for air as the working gas (1 atm). It is obvious from the schematic of Fig. 3 that the emphasis for this calculation is on the tail flame of the RF plasma.

As an example, Fig. 4 shows temperature and flow fields for a plasma power of 25 kW. As the power level increases, the maximum temperature (approximately 11,000 K) remains almost the same as in case 1, but again, the hot plasma expands somewhat farther downstream and, at the same time, the velocity in the tail flame increases substantially as shown in Fig. 5. This leads to a substantial increase of the enthalpy far downstream from the exit nozzle (see Fig. 6).

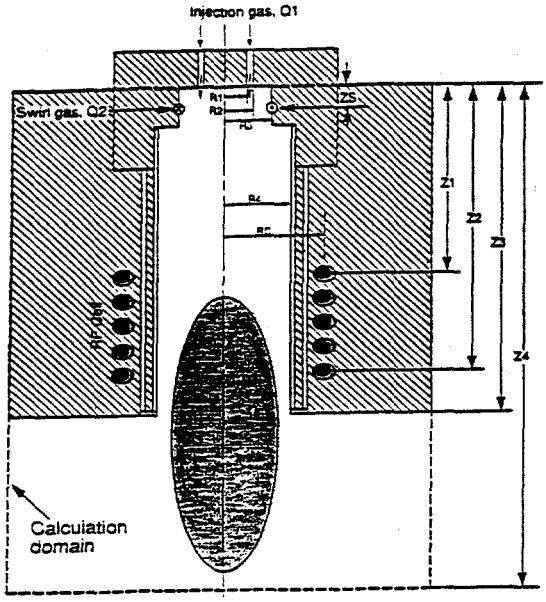

Fig. 3: Schematic of the RF plasma torch and the calculation domain (Case 2)

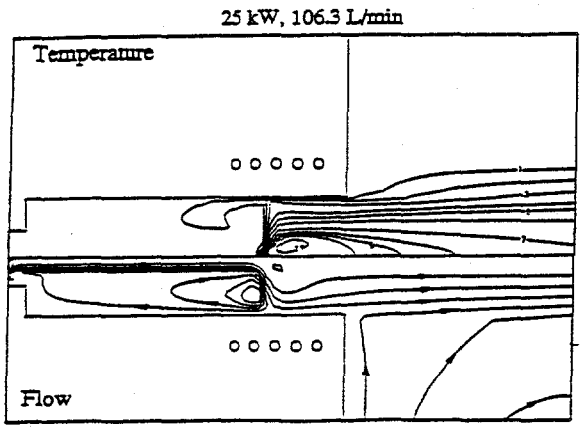

Fig. 4: Temperature and flow profiles of the air plasma torch

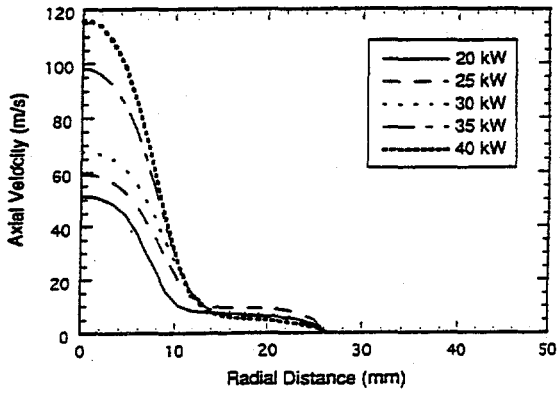

Fig. 5: Axial velocities at the downstream end of the coil

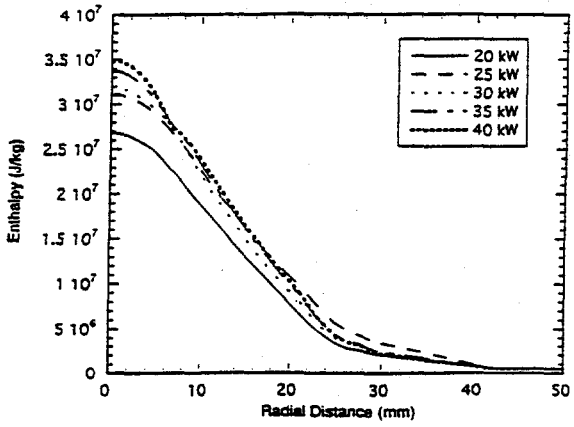

Fig. 6: Enthalpy profiles far downstream from the torch exit

DIAMOND DEPOSITION EXPERIMENTS WITH LIQUID PRECURSORS.

We have previously reported results of experiments in which very high growth rates of diamond films have been obtained by injecting liquids in form of an atomized jet in a counterflow arrangement into a plasma jet [10]. Liquids used in these studies included a variety of organics including PCB contaminated oils. We had demonstrated that jet fluctuations could lead to film non-uniformities. In order to obtain a better understanding of this deposition process, controlled experiments were performed in which the effect of mass transport was investigated. These investigations included (a) determination of the droplet size for different liquids using our atomizing nozzle in a particle size diagnostics wind tunnel, (b) an analysis of the evaporation behavior of the different liquid droplets used, and (c) observation of the droplet trajectories in the reactor for counterflow injection and for injection from the side parallel to the substrate. The specific liquids investigated were acetone, ethanol and toluene. It was found that differences in the physical characteristics of these liquids did not influence the mass transport to the substrate. The droplet trajectories were observed with the laser strobe video system. A new reactor had to be designed for this purpose with windows which would allow laser beam access and observation of the reflected signal without disturbing the flow pattern in the reactor. Fig. 7 shows schematically the set-up of the laser strobe video system. The electronic shutter of the CCD video head opens for 50 ns during which the nitrogen laser delivers a pulse. The light reflected by the droplets passes through a narrow line filter to block out background radiation and is captured by the video head. The images are recorded on tape and are then processed by computerized image analysis. Fig. 8 shows a computer enhanced image of droplets injected from the side 5 mm above the substrate interacting with the plasma jet coming from the top of the picture. It is apparent that droplets nearly reach the substrate providing efficient mass transport. We have found a dependence of growth rate on the plasma torch power, indicating that the diamond film growth may be limited by the amount of atomic hydrogen provided by the plasma jet. One observation which we cannot explain at present is that the diamond crystal size is quite different when different precursors are used. Fig. 9 shows SEM photos of films obtained with acetone and with ethanol, indicating the larger crystal size obtained with ethanol.

In order to guide further diagnostic experiments, we have initiated the modeling effort which includes description of the droplet formation, droplet - jet interaction, and the surface chemistry.

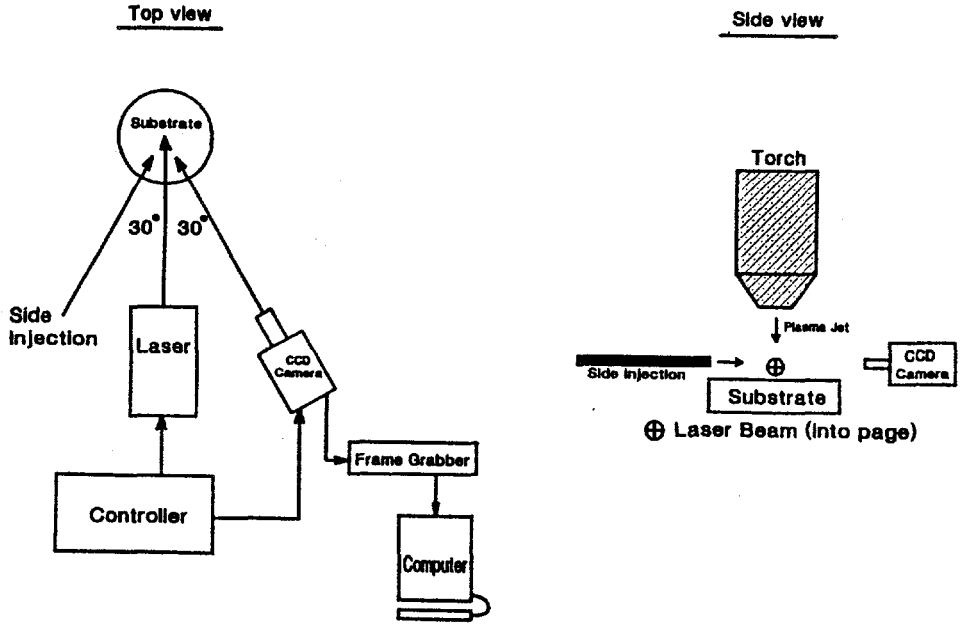

Fig. 7: Schematic of liquid droplet injection reactor and of laser strobe video set-up.

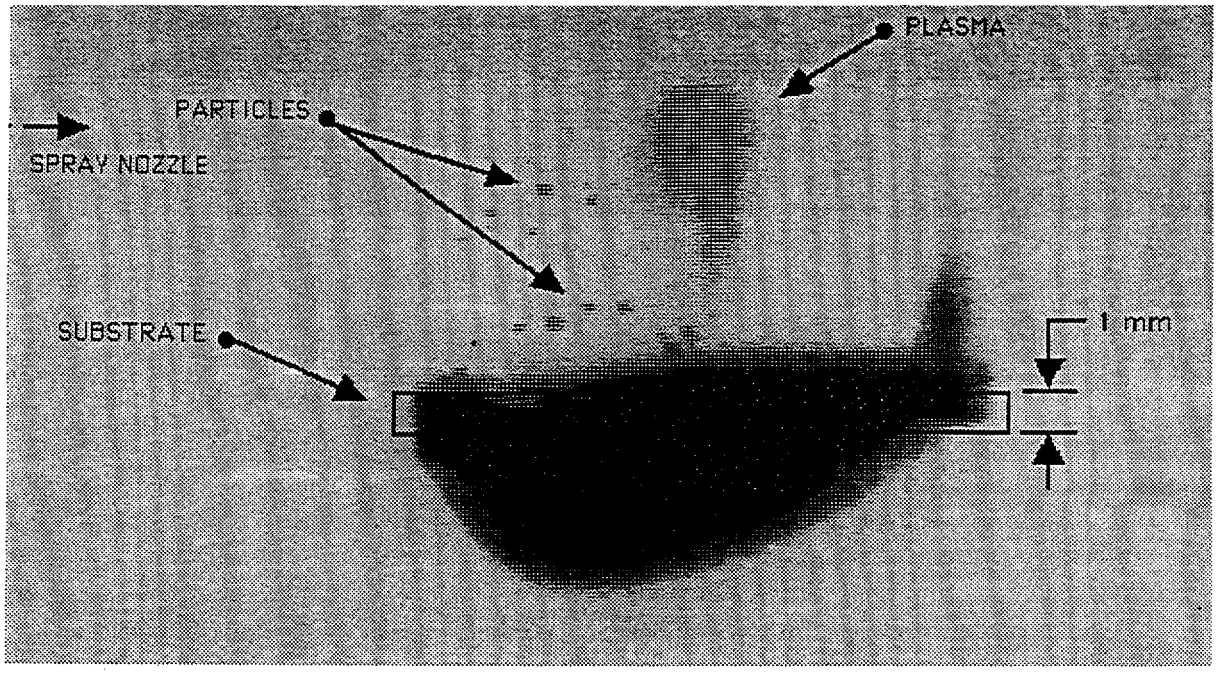

Fig. 8: Computer enhanced video image of plasma jet (center top) and of liquid droplets (injected from the left). The dark region in the center is a reflection from the substrate.
Injection probe position: 3 mm above the substrate;
Liquid: ethanol; atomizing gas: hydrogen;
Torch power: 10.5 kW.

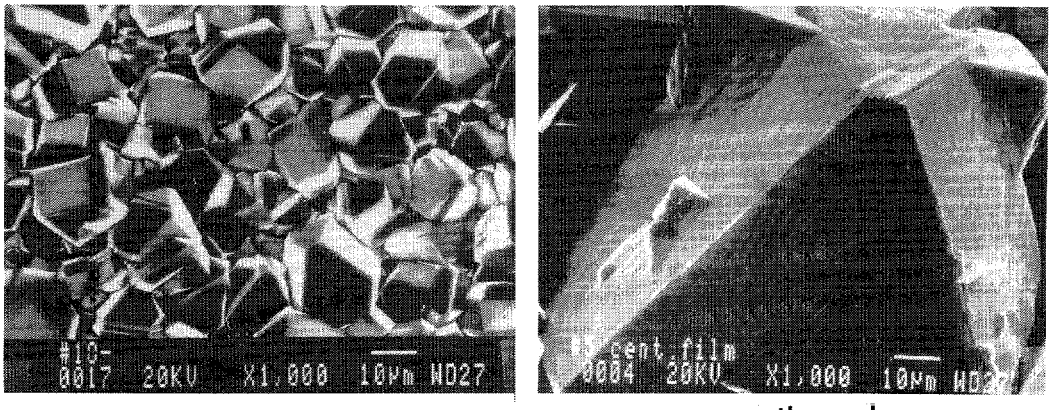

acetone ethanol

Fig. 9: Scanning Electron Micrographs of diamond films obtained from acetone and from ethanol with side injection for identical torch operating conditions.

CONCLUSIONS

Modeling of inductively-coupled RF plasmas indicates that with oxygen or air as the working gas, the maximum temperature in the plasma remains almost the same (around 11,000 K), regardless of the power input to the plasma. The hot plasma, however, extends farther downstream as the power input increases and, at the same time, the velocity in the plasma tail flame increases for the same mass flow rate. The quantitative description of the process details allow the derivation of scaling laws for process reactor design.

For a better understanding of the unusually high growth rates (up to mm/hr) of diamond films observed with liquid precursors injected into a thermal plasma jet, droplet visualization tests have been made, using a laser strobe system. The results show that the plasma jet accelerates the droplets towards the substrate, and some of the droplets almost reach the substrate surface, providing an efficient transport of chemically active species to the surface. The availability of atomic hydrogen seems to be a limiting factor for diamond growth in this case. The size of the well-faceted diamond crystals varies with different precursor materials (acetone, ethanol, benzene, etc.), an observation which remains unexplained at this point. Modeling of this process is necessary to enhance our understanding of the process details and to allow us to make full use of the high diamond film growth rates.

ACKNOWLEDGMENTS

The contributions by Mr. D. Or to the rf plasma modeling, and by Dr. D. Zhuang and Mr. P. Schwendinger to the characterization of the liquid injection reactor are gratefully acknowledged. This work has been supported by DOE under grant No.DOE/F602-85ER-13433.

REFERENCES

1. E. Pfender, J. Fincke, R. Spores, "Entrainment of Cold Gas into Thermal Plasma Jets", *Plasma Chem. Plasma Process.* **11**, 529-543 (1991).
2. W.L.T. Chen, J. Heberlein, and E. Pfender, "Diagnostics of a Thermal Plasma Jet by Optical Emission Spectroscopy and Enthalpy Probe Measurements," Plasma Chemistry and Plasma Processing, Vol. 14(3), pp. 317-332 (1994).
3. S,C. Snyder, L.D. Reynolds, J.R. Fincke, G.D. Lassahn, J.D. Grandy, T.E. Repetti, Electron-temperature and electron-density profiles in an atmospheric-pressure argon plasma jet," *Phys.Rev. E*, 50/1, 519-525 (1994).
4. G.Y. Zhao, J. Mostaghimi and M.I. Boulos, "The Induction Plasma Chemical Reactor, Part I: Equilibrium Model", *Plasma Chem. Plasma Process.* **10**, 133-150 (1990).
5. G.Y. Zhao, J. Mostaghimi and M.I. Boulos, "The Induction Plasma Chemical Reactor, Part II: Kinetic Model", *Plasma Chem. Plasma Process.* **10**, 151-166 (1990).
6. X. Chen and E. Pfender, "Modeling of RF Plasma Torch with a Metallic Tube Inserted for Reactant Injection", *Plasma Chemistry and Plasma Processing*, **11** (1), (1991).
7. C.K.G. Lam and K.A. Bremhorst, "Modified Form of the k-ε Model for Predicting Wall Turbulence", *J. Fluids Engineering*, **103**, 456 (1981).
8. W.P. Jones and B.E. Launder, "The Prediction of Laminarization with a Two-Equation Model of Turbulence", *Int. J. Heat Mass Transfer*, **15**, 301 (1972).
9. S.V. Patankar, *Numer. Heat Transfer Fluid Flow*, New York: McGraw Hill (1980).
10. E. Pfender, Q.Y. Han, T.W. Or, Z.P. Lu, and J. Heberlein, "Rapid synthesis of diamond by counter-flow liquid injection into an atmospheric pressure plasma jet," Diamond and Related Materials, Vol.1 (1), p.127, 1992.

HYDRODYNAMIC THEORY OF DIFFUSION IN TWO-TEMPERATURE MULTICOMPONENT PLASMAS

J. D. Ramshaw and C. H. Chang

Idaho National Engineering Laboratory
Idaho Falls, ID 83415

ABSTRACT

Detailed numerical simulations of multicomponent plasmas require tractable expressions for species diffusion fluxes, which must be consistent with the given plasma current density $\mathbf{J}_q$ to preserve local charge neutrality. The common situation in which $\mathbf{J}_q = \mathbf{0}$ is referred to as ambipolar diffusion. The use of formal kinetic theory in this context leads to results of formidable complexity. We derive simple tractable approximations for the diffusion fluxes in two-temperature multicomponent plasmas by means of a generalization of the hydrodynamical approach used by Maxwell, Stefan, Furry, and Williams. The resulting diffusion fluxes obey generalized Stefan-Maxwell equations that contain driving forces corresponding to ordinary, forced, pressure, and thermal diffusion. The ordinary diffusion fluxes are driven by gradients in pressure fractions rather than mole fractions. Simplifications due to the small electron mass are systematically exploited and lead to a general expression for the ambipolar electric field in the limit of infinite electrical conductivity. We present a self-consistent effective binary diffusion approximation for the diffusion fluxes. This approximation is well suited to numerical implementation and is currently in use in our LAVA computer code for simulating multicomponent thermal plasmas. Applications to date include a successful simulation of demixing effects in an argon-helium plasma jet, for which selected computational results are presented. Generalizations of the diffusion theory to finite electrical conductivity and nonzero magnetic field are currently in progress.

INTRODUCTION

There is a growing interest in the use of thermal plasmas for materials processing and synthesis applications. This has stimulated a parallel interest in the development and application of physical models and numerical methods for performing detailed space- and time-resolved

simulations of such plasmas [1,2]. Thermal plasmas are inherently multicomponent systems, so constitutive relations for the diffusional mass fluxes in the plasma are an essential ingredient in such models. Forced diffusion due to the electric field $\mathbf{E}$ is in turn an essential contribution to the diffusion fluxes. Even in the absence of an external electric field, an internal field spontaneously arises to preserve local charge neutrality, which would otherwise be disrupted by the natural tendency of the very light electrons to rapidly diffuse away from the much heavier ions and neutral atoms. The electric field is the mechanism by which the diffusion fluxes are constrained to produce an electrical current density $\mathbf{J}_q$ which preserves local charge neutrality. This implies $\nabla \cdot \mathbf{J}_q = \mathbf{0}$ at a minimum, but in many cases the stronger condition $\mathbf{J}_q = \mathbf{0}$ is satisfied. Diffusion in this latter situation is referred to as ambipolar diffusion [3].

Ambipolar diffusion in simple situations is treated in textbooks, but the resulting expressions are inadequate to deal with the arbitrary multicomponent mixtures of present concern. The required general expressions could in principle be derived from the kinetic theory of gases, but this theory is usually developed under the assumption that all the species or components share a common translational temperature. This assumption is frequently violated in thermal plasmas, where a variety of nonequilibrium effects can cause the electron temperature T_e to be significantly different from the heavy-particle temperature T [2]. This complication presents formidable difficulties in the kinetic theory, and is a serious obstacle to the development of simple and tractable approximations for the diffusion fluxes. We have therefore pursued an alternative hydrodynamic approach [4] which captures the essential physics within a much simpler and more transparent framework, and permits the derivation of a simple multitemperature ambipolar diffusion formulation [5] suitable for practical calculations and numerical implementation.

The hydrodynamic theory of diffusion has a distinguished history dating back to Maxwell and Stefan [6,7], and has been further elaborated in more recent times by Furry [8], Williams [9], and Ramshaw [4]. This theory has largely been superseded by the more accurate treatment made possible by the general kinetic theory of gases [6,10], but the latter theory has the disadvantage of being much more intricate and complex. For this reason, the hydrodynamic theory still retains value as a simple and physically transparent approach which leads to essentially correct results in a very straightforward manner. Indeed, the results of the hydrodynamic theory are surprisingly accurate; in the special case when $T_e = T$, they are in precise agreement with first-order Chapman-Enskog theory [4].

THE MULTITEMPERATURE STEFAN-MAXWELL EQUATIONS

The starting point of the hydrodynamic theory of diffusion is a conventional multifluid description with separate continuity and momentum equations for each of the N species in the mixture. These momentum equations contain frictional terms proportional to species velocity differences and thermophoretic force terms proportional to temperature gradients [4]. A reduction of the multifluid description to a diffusional description results when the friction coefficients are large, so that the slip velocities between species are reduced to very small values. The separate species accelerations then become very nearly equal to the mean acceleration of the plasma as a whole, whereupon the species momentum equations reduce to Stefan-Maxwell equations of the form [4]

$$\sum_j \frac{z_i z_j}{D_{ij}} (\mathbf{u}_j - \mathbf{u}_i) = \mathbf{H}_i - \left(\frac{\rho_i q_i}{p} \right) \mathbf{E} \tag{1}$$

where $z_i = p_i/p$, p_i is the partial pressure of species i, $p = \sum_i p_i$ is the total pressure, D_{ij} is the binary diffusion coefficient for the pair (i,j) (which depends on an effective pair temperature $T_{ij} = (m_i T_j + m_j T_i)/(m_i + m_j)$, where T_i and m_i are respectively the temperature and molecular mass of species i [4]), $\mathbf{u}_i$ is the specific velocity of species i, $\mathbf{H}_i = \nabla z_i + (z_i - y_i)\nabla \ln p + \mathbf{K}_i$, ρ_i and q_i are respectively the partial mass density and charge per unit mass of species i, $y_i = \rho_i/\rho$, $\rho = \sum_i \rho_i$ is the total mass density, $\mathbf{K}_i$ represents thermophoretic force terms proportional to temperature gradients [4], and we have assumed that the only external forces present are those of gravity (which cancels out) and the electric field. It is noteworthy that Eqs. (1) have the same form as the usual single-temperature Stefan-Maxwell equations [10], but with the mole fractions x_i replaced by the corresponding pressure fractions z_i. In the present context, all the heavy species have the same common temperature T, so that $T_i = T$ for $i \neq e$, while $T_i = T_e$ for $i = e$.

Only $N - 1$ of Eqs. (1) are linearly independent, as their sum over i yields $\mathbf{0} = \mathbf{0}$. These equations contain $N + 1$ unknowns, namely the $\mathbf{u}_i$ and $\mathbf{E}$. The two additional equations needed to close the system are

$$\sum_i \rho_i \mathbf{u}_i = \rho \mathbf{u} \tag{2}$$

$$\sum_i \rho_i q_i \mathbf{u}_i = \mathbf{J}_q \tag{3}$$

where $\mathbf{u}$ is the mass-averaged plasma velocity determined by the mean momentum equation, and $\mathbf{J}_q = \mathbf{0}$ in the ambipolar case. Equations (1)–(3) constitute a system of $N + 1$ linear equations for the $\mathbf{u}_i$ and $\mathbf{E}$, which must in general be solved at each point in space and time. The resulting $\mathbf{u}_i$ then determine the species diffusion fluxes $\mathbf{J}_i = \rho_i(\mathbf{u}_i - \mathbf{u})$, which in turn determine the time evolution of the ρ_i via the species continuity equations [4].

SIMPLIFICATIONS DUE TO SMALL ELECTRON MASS

The diffusion coefficients D_{ij} are of order $\mu_{ij}^{-1/2}$, where $\mu_{ij} = m_i m_j/(m_i + m_j)$. Since $m_e \ll m_j$ $(j \neq e)$, it follows that $\mu_{ej} \cong m_e$ and $D_{ej} \sim m_e^{-1/2}$. The entire left member of Eq. (1) for $i = e$ is therefore of order $m_e^{1/2}$, which is very small and may ordinarily be neglected. We thereby obtain

$$\mathbf{E} = \frac{p}{\rho_e q_e} \mathbf{H}_e \tag{4}$$

which is a general expression for the ambipolar electric field in an arbitrary two-temperature multicomponent plasma. It may now be used to eliminate $\mathbf{E}$ from Eq. (1) for $i \neq e$, in which the term $j = e$ may now be omitted from the summation as it is also of order $m_e^{1/2}$. The $i = e$ term in Eq. (2) may be omitted *a fortiori*, as it is of order m_e. When all this is done, Eqs. (1) (for $i \neq e$) and (2) no longer involve $\mathbf{u}_e$, and only $N - 2$ of Eqs. (1) for $i \neq e$ remain linearly independent. These equations, together with Eq. (2), then constitute a linear system of $N - 1$ equations for the $N - 1$ unknowns $\mathbf{u}_i$ with $i \neq e$. The final unknown $\mathbf{u}_e$ is then determined by Eq. (3).

The electrical conductivity of the plasma is of order $m_e^{-1/2}$ [6], so the resistivity is of order $m_e^{1/2}$. By neglecting terms of order $m_e^{1/2}$, we have effectively approximated the resistivity by zero; *i.e.*, the plasma has been approximated as a perfect conductor. Indeed, Eq. (4) for $\mathbf{E}$ may be interpreted as the generalized Ohm's law for the plasma in the limit of infinite conductivity.

THE SELF-CONSISTENT EFFECTIVE BINARY DIFFUSION APPROXIMATION

Self-consistent effective binary diffusion approximations are frequently used to avoid solving the linear system of Eqs. (1)–(3). A rational basis for such approximations has recently been presented [11] and applied in the present context [3–5]. In the limit of small electron mass, the resulting expressions for the $\mathbf{J}_i$ ($i \neq e$) take the form [5]

$$\mathbf{J}_i = \mathbf{J}_i^0 - y_i \sum_{j \neq e} \mathbf{J}_j^0 \tag{5}$$

where

$$\mathbf{J}_i^0 = -\frac{m_i D_i}{k_B T}(p\mathbf{H}_i - \rho_i q_i \mathbf{E}) \tag{6}$$

where k_B is Boltzmann's constant. These equations provide explicit approximate expressions for the diffusion fluxes of the heavy species. The diffusion flux for the electrons is then determined by Eq. (3). Notice that Eqs. (5) and (6) involve the effective binary diffusivities D_i [11] and temperature T for the heavy species only. They are therefore well suited for numerical implementation, where the very large value of D_e might otherwise have given rise to unacceptably restrictive stability and/or accuracy restrictions. These equations are currently in use in our LAVA computer code for simulating nonequilibrium thermal plasma processes [1,2]. Some illustrative computational results are presented in the next section.

DEMIXING IN ARGON-HELIUM PLASMA JETS

Demixing effects in plasma torches [12] provide a particularly interesting example of multicomponent diffusive phenomena in thermal plasmas. For example, in an argon-helium plasma jet discharging into quiescent air, the helium mole fraction in the jet core at the torch exit is substantially enhanced relative to the premixed feed gas due to diffusive demixing in the discharge region [12]. This effect results from an interplay between diffusion and ionization. The ionization potential of argon (15.8 eV) is considerably lower than that of helium (24.6 eV), so the argon is preferentially ionized near the torch centerline where the temperature is highest. This creates radial concentration gradients in both argon ions and electrons, resulting in radial outward ambipolar diffusion of argon ions. In addition, each ionization event produces two particles from one, which reduces the helium mole fractions near the centerline. This causes helium to diffuse radially inward, resulting in an enrichment of helium near the centerline and a corresponding depletion near the torch wall. The degree of demixing is primarily determined in the discharge region, but the diffusional separation process continues to operate for some distance downstream of the nozzle exit. Eventually, however, recombination occurs as temperatures drop and the argon and helium remix to regenerate the initial mixture ratio.

A suitable formulation for multicomponent ambipolar diffusion is essential to an accurate physical description of this and similar effects involving coupling between concentrations and diffusion fluxes of individual ionized and neutral species. Previous simplified approaches, such as those in which the plasma is approximated as a two-component mixture of the plasma gas and air [13,14], are fundamentally incapable of capturing such effects, as they neglect individual species diffusion fluxes as well as interactions between the multiple dissociation and ionization reactions occurring in the plasma. For example, ionization of argon is suppressed by the electrons produced by ionization of other species. Ionization processes are highly energetic and strongly

temperature dependent, so interaction effects of this type are essential to a quantitative description of multicomponent thermal plasmas.

The present ambipolar diffusion formulation, as implemented in the LAVA code [1,2], has been used to perform detailed numerical simulations of demixing in argon-helium plasma jets and comparisons with corresponding experimental data [12]. LAVA is a fluid-dynamical model which represents the plasma as an ideal gas mixture with temperature-dependent specific heats and transport properties. The equations solved consist of the mixture momentum equation for the plasma, separate thermal internal energy equations for the mixture and electrons, continuity equations for each component of the mixture, ideal-gas state relations, chemical kinetic rate expressions, and transport equations for turbulence parameters. The numbers of components and chemical reactions are arbitrary. Detailed descriptions of the theoretical model and numerical scheme are available elsewhere [1,2].

The present simulations were performed in two-dimensional cylindrical coordinates, as the plasma torch is presumed to be axisymmetric. Gravity and swirl were neglected, and complete local thermodynamic equilibrium (LTE) was assumed. This implies both chemical and thermal equilibrium, so the electron and heavy-particle temperatures were taken to be equal. Eleven species were included in the calculations, namely Ar, Ar^+, e^-, He, He^+, N_2, N, N^+, O_2, O, and O^+. The formation of NO_x is neglected due to the fact that negligible amounts were observed experimentally. The following six chemical reactions were included: The chemical reactions are

$$\begin{aligned} Ar &\rightleftharpoons Ar^+ + e^- \\ He &\rightleftharpoons He^+ + e^- \\ N_2 &\rightleftharpoons 2N \\ O_2 &\rightleftharpoons 2O \\ N &\rightleftharpoons N^+ + e^- \\ O &\rightleftharpoons O^+ + e^- \end{aligned}$$

all of which are assumed to be in equilibrium.

The geometry and operating conditions of the plasma torch are typical of a commercial unit (Miller SG-100). This torch has an 8 mm nozzle exit diameter and was operated subsonically. Torch operating conditions for the data presented are 800 A at 37 V, for a total power input of 29.6 kW, approximately 2/3 of which is deposited in the torch gas. The argon and helium flow rates were 3200 ℓ/hr and 1331 ℓ/hr respectively, resulting in a premixed [Ar]/[He] mixture ratio of 2.4. The inflow profiles of Ar and He concentrations, velocity, and temperature at the torch exit were obtained from the experimental data 0.5 cm from the nozzle exit [12].

Figure 1 shows the computed and experimental argon/helium cold mole fraction ratios along the centerline. The experimental results were obtained by enthalpy probe measurements using a differentially pumped quadrapole mass spectrometer system to determine species concentrations [12]. The cold mole fraction of argon is defined by

$$x^c_{Ar} = \frac{[Ar] + [Ar^+]}{[Ar] + [Ar^+] + [He] + [He^+] + [N_2] + [O_2] + \frac{1}{2}([N] + [N^+] + [O] + [O^+])} \qquad (7)$$

where [X] is the molar concentration of species X in the plasma. This is the argon mole fraction measured by sampling the plasma and cooling it to room temperature at constant elemental composition. The cold mole fractions of helium and air are given by analogous expressions.

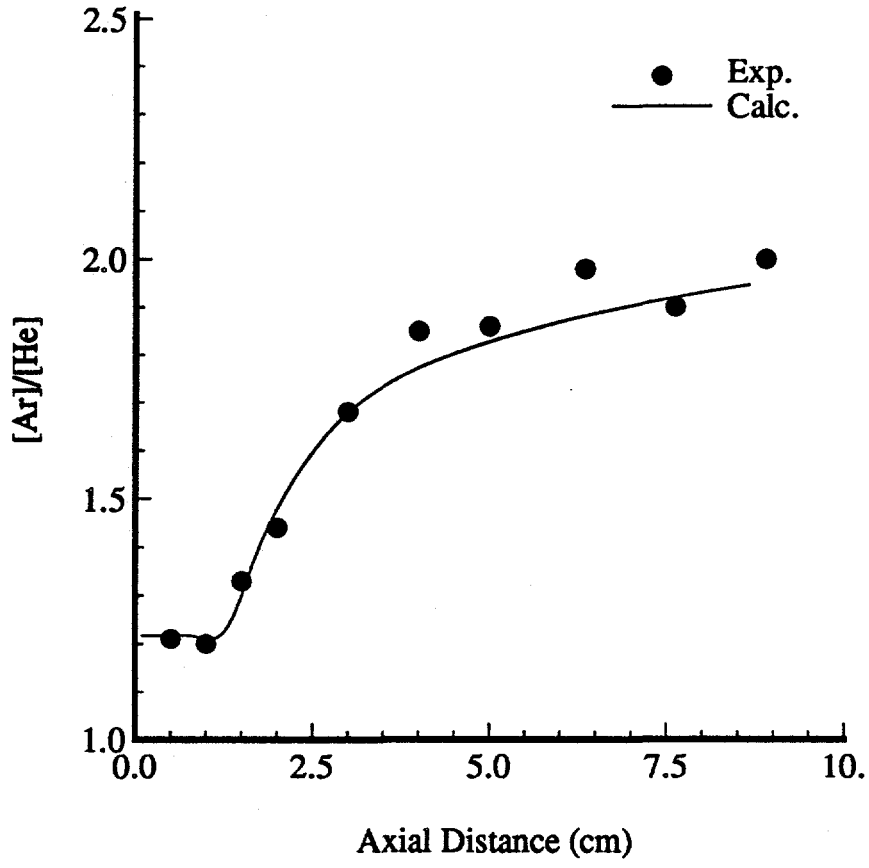

Figure 1. Calculated and Experimental Argon to Helium Cold Mole Fraction Ratio Along the Centerline.

Figure 1 shows that the centerline argon/helium cold mole fraction ratio is approximately 1.2 at the 0.5 cm axial location. This ratio is 2.4 for the premixed plasma gas, so the diffusive demixing effect is quite dramatic. The experimental data show a slight further decrease in this ratio between 0.5 cm and 1.0 cm, indicative of continued diffusive demixing in this region. Note that the simulation also captures this effect. Beyond 1.0 cm, the plasma rapidly cools and remixing again begins to occur, as discussed above.

Figure 2 shows radial plots of the Ar-He cold mole fraction ratio at axial locations of 0.5 cm (inflow condition), 2.0 cm, and 5.0 cm. After the shear layer surrounding the jet encroaches into the centerline (which occurs at about 1.0 cm [12]), turbulent mixing overcomes diffusive demixing and the Ar-He ratio begins to increase again. By 5.0 cm, the profile of Ar-He mole fraction ratio has been flattened by the mixing process and is approaching a value of about 2.0 on the centerline.

ACKNOWLEDGMENTS

We are grateful to Jim Fincke for helpful discussions and collaboration. This work was performed under the auspices of the U. S. Department of Energy under DOE Field Office, Idaho Contract DE-AC07-94ID13223, supported by the U. S. Department of Energy, Office of Energy Research, Office of Basic Energy Sciences, Division of Engineering and Geosciences.

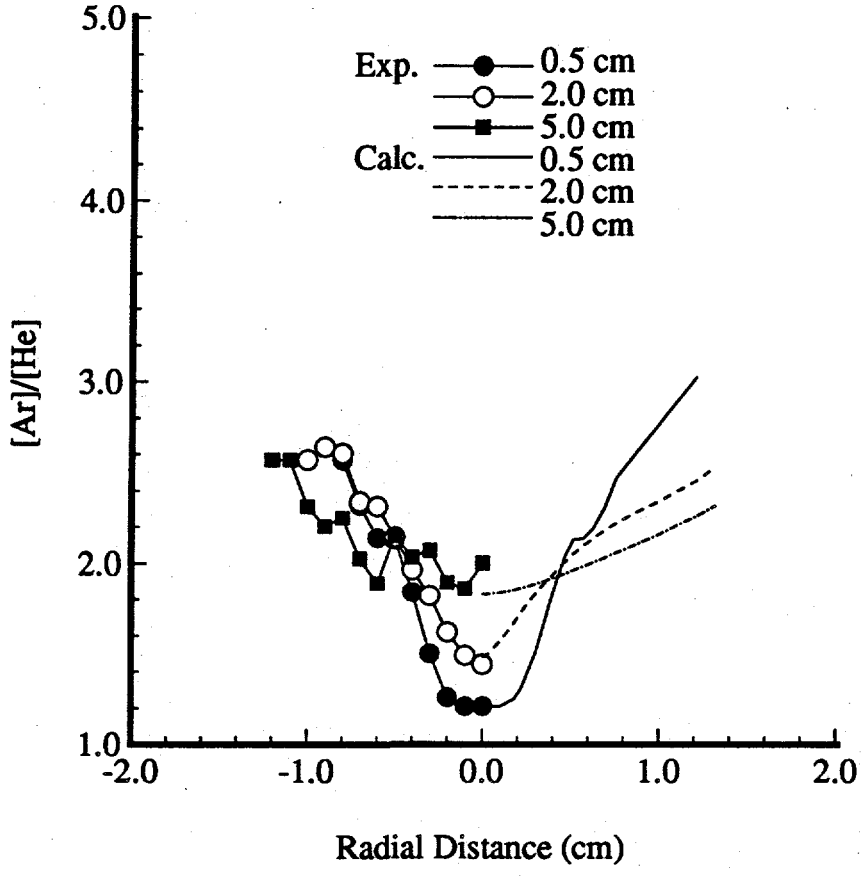

Figure 2. Calculated and Experimental Radial Profiles of Argon to Helium Cold Mole Fraction Ratio.

REFERENCES

1. J. D. Ramshaw and C. H. Chang, "Computational Fluid Dynamics Modeling of Multicomponent Thermal Plasmas," *Plasma Chem. Plasma Process.* **12**, 299 (1992).

2. C. H. Chang and J. D. Ramshaw, "Numerical Simulation of Nonequilibrium Effects in an Argon Plasma Jet," *Phys. Plasmas* **1**, 3698 (1994).

3. J. D. Ramshaw and C. H. Chang, "Ambipolar Diffusion in Multicomponent Plasmas," *Plasma Chem. Plasma Process.* **11**, 395 (1991).

4. J. D. Ramshaw, "Hydrodynamic Theory of Multicomponent Diffusion and Thermal Diffusion in Multitemperature Gas Mixtures," *J. Non-Equilib. Thermodyn.* **18**, 121 (1993).

5. J. D. Ramshaw and C. H. Chang, "Ambipolar Diffusion in Two-Temperature Multicomponent Plasmas," *Plasma Chem. Plasma Process.* **13**, 489 (1993).

6. S. Chapman and T. G. Cowling, *The Mathematical Theory of Non-Uniform Gases,* 3rd ed. Cambridge University Press, Cambridge, UK (1970).

7. C. Truesdell, "Mechanical Basis of Diffusion," *J. Chem. Phys.* **37**, 2336 (1962).

8. W. H. Furry, "On the Elementary Explanation of Diffusion Phenomena in Gases," *Am. J. Phys.* **16**, 63 (1948).

9. F. A. Williams, "Elementary Derivation of the Multicomponent Diffusion Equation," *Am. J. Phys.* **26**, 467 (1958).

10. J. O. Hirschfelder, C. F. Curtiss, and R. B. Bird, *Molecular Theory of Gases and Liquids,* Wiley, New York (1964).

11. J. D. Ramshaw, "Self-Consistent Effective Binary Diffusion in Multicomponent Gas Mixtures," *J. Non-Equilib. Thermodyn.* **15**, 295 (1990).

12. J. R. Fincke, C. H. Chang, W. D. Swank, and D. C. Haggard, "Entrainment and Demixing in Subsonic Thermal Plasma Jets: Comparison of Measurements and Predictions," *Int. J. Heat Mass Transfer* **37**, 1673 (1994).

13. Y. P. Chyou and E. Pfender, "Modeling of Plasma Jets with Superimposed Vortex Flow," *Plasma Chem. Plasma Process.* **9**, 291 (1989).

14. A. H. Dilawari, J. Szekely, and R. Westhoff, "A Comparison of Experimental Measurements and Theoretical Predictions Regarding the Behavior of a Turbulent Argon Plasma Jet Discharging into Air," *Plasma Chem. Plasma Process.* **10**, 501 (1990).

Final List of Participants

THIRTEENTH SYMPOSIUM ON ENERGY ENGINEERING SCIENCES

May 15-17, 1995

Argonne National Laboratory
Argonne, Illinois

Guenter Ahlers
University of California-Santa Barbara
Department of Physics
Santa Barbara, CA 93106

Chong H. Chang
Idaho National Engineering Laboratory
P.O. Box 1625, Mail Stop 3808
Idaho Falls, ID 83415

Paul I. Barton
Massachusetts Institute of Technology
Department of Chemical Engineering
Room 66-464
Cambridge, MA 02139

Ezechiel G. D. Cohen
The Rockefeller University
Physics Department
1230 York Avenue
New York, NY 10021-6399

Haim H. Bau
University of Pennsylvania
Department of Mechanical Engineering
Philadelphia, PA 19104-6315

Eiichi Fukushima
The Lovelace Institutes
2425 Ridgecrest Drive SE
Albuquerque, NM 87108

Frederick W. Brust, Jr.
Battelle
Engineering Mechanics Group
505 King Avenue
Columbus, OH 43201-2693

Robert Goulard
George Washington University
SEAS Department
801 22nd Street NW
Washington, DC 70052

Brent D. Butler
NIST
Chemical Sciences & Tech. Lab, Thermophysics Div.
325 Broadway
Boulder, CO 80303

Howard J. M. Hanley
NIST
Thermophysics Division
325 Broadway
Boulder, CO 80303

Shrikar Chakravarti
University of Wisconsin-Madison
Department of Chemical Engineering
1415 Johnson Drive
Madison, WI 53706-1691

Thomas J. Hanratty
University of Illinois
Department of Chemical Engineering
205 Roger Adams Laboratory
600 South Mathews
Urbana, IL 61801

Shawn G. Hausen
Northwestern University
Department of Chemical Engineering
2145 Sheridan Road
Evanston, IL 60208

Oscar Manley
U.S. Department of Energy
Division of Engineering and Geosciences
Office of Basic Energy Sciences, ER-15
Washington, DC 20585

Joachim V. R. Heberlein
University of Minnesota
Department of Mechanical Engineering
111 Church Street SE
Minneapolis, MN 55455

John B. McLaughlin
Clarkson University
Department of Chemical Engineering
Potsdam, NY 13699-5705

Frank P. Incropera
Purdue University
School of Mechanical Engineering
1288 Mechanical Engineering Building
West Lafayette, IN 47907

Eckart H. Meiburg
University of Southern California
Department of Aerospace Engineering
Los Angeles, CA 90089-1191

Daniel Kaftori
University of California-Santa Barbara
Dept. of Chemical & Nuclear Eng., Mechanical Eng.
Santa Barbara, CA 93106

Curtis R. Menyuk
University of Maryland-Baltimore County
Department of Electrical Engineering
TRC 201A
Baltimore, MD 21228-5398

Robert H. Kraichnan
369 Montezuma 108
Santa Fe, NM 87501

Issam Mudawar
Purdue University
Department of Mechanical Engineering
1288 Mechanical Engineering
West Lafayette, IN 47907

Allan J. Lichtenberg
University of California
Dept. of Electrical Engineering and Comp. Sci.
Cory Hall
Berkeley, CA 94720

Evgeny A. Novikov
University of California-San Diego
Institute for Nonlinear Science
La Jolla, CA 92093-0402

Julio M. Ottino
Northwestern University
Department of Chemical Engineering
2145 Sheridan Road
Evanston, IL 60208

George Schmidt
Stevens Institute of Technology
Department of Physics & Engineering Physics
Hoboken, NJ 07030

Thomas G. Owano
Stanford University
Department of Mechanical Engineering
Bldg. 520, Rm. 521Q
Stanford, CA 94305-3032

Daphne L. Stoner
Idaho National Engineering Laboratory
Department of Biotechnology
Lockheed Idaho Technologies Company
2351 North Boulevard, P.O. Box 1625
Idaho Falls, ID 83415

Walter Polansky
U.S. Department of Energy
Advanced Energy Projects Division, ER-33
19901 Germantown Road
Germantown, MD 20874-1290

Harry L. Swinney
University of Texas-Austin
Center for Nonlinear Dynamics
Austin, TX 78712

Gerald C. Pomraning
University of California-Los Angeles
Department of Mechanical, Aerospace, and Nuclear
405 Hilgard Avenue
Los Angeles, CA 90024-1597

Stephen L. Teitel
University of Rochester
Department of Physics and Astronomy
Rochester, NY 14627

W. Harmon Ray
University of Wisconsin
Department of Chemical Engineering
1415 Johnson Drive
Madison, WI 53706

Chang-Lin Tien
University of California-Berkeley
Office of the Chancellor
200 California Hall #1500
Berkeley, CA 94720-1500

John Ross
Stanford University
Department of Chemistry
Stanford, CA 94305

Salvatore Torquato
Princeton University
Department of Civil Engineering
Princeton Materials Institute
Princeton, NJ 08544

James M. Wallace
The University of Maryland
Department of Mechanical Engineering
College Park, MD 20742

Graham B. Wallis
Dartmouth College
Thayer School of Engineering
Hanover, NH 03755-8000

James R. Welty
U.S. Department of Energy
Division of Engineering and Geosciences
Office of Basic Energy Sciences, ER-15
Washington, DC 20585

Arthur W. Westerberg
Carnegie Mellon University
Department of Chemical Engineering
5000 Forbes Avenue
Pittsburgh, PA 15213